LOI12-18-002

A Run-Group Letter-Of-Intent Submitted to PAC 46

Deeply Virtual Compton Scattering using the Tagged Deeply Inelastic Scattering Experimental Setup

DRAFT: June 4, 2018

Alexandre Camsonne (*spokesperson*), Marco Carmignotto (*spokesperson*), Silviu Covrig Dusa

Thomas Jefferson National Accelerator Facility, Newport News, VA, USA

Zhihong Ye (*spokesperson*)

Argonne National Laboratory, Lemont, IL, USA

Eric Fuchey (*spokesperson*) †, Andrew Puckett (*spokesperson*)

University of Connecticut, Storrs, CT, USA

Rachel Montgomery (*spokesperson*)

University of Glasgow, Glasgow, UK

Zhenyu Ye (*spokesperson*)

University of Illinois at Chicago, Chicago, IL, USA
spokesperson)

Kondo Gnanvo, Nilanga Linayage, Huong Nguyen

University of Virginia, Charlottesville, VA, USA
Mitra H. Shabestari

Mississippi State University, MS, USA

Kijun Park

Hampton University, Hampton, VA, USA

and the Hall A SBS collaboration.

†contact person
(

Abstract

We are proposing to study the deeply virtual Compton scattering in parallel to the TDIS experiment. This would constitute the first measurement of DVCS using the Super BigBite spectrometer. This will complement the other measurements on the proton and most interestingly the deuterium target data which can yield the DVCS process on both the neutron and DVCS process on the coherent deutons thanks to the availability of a TPC as a recoil detector.

Contents

1 Introduction and Motivations

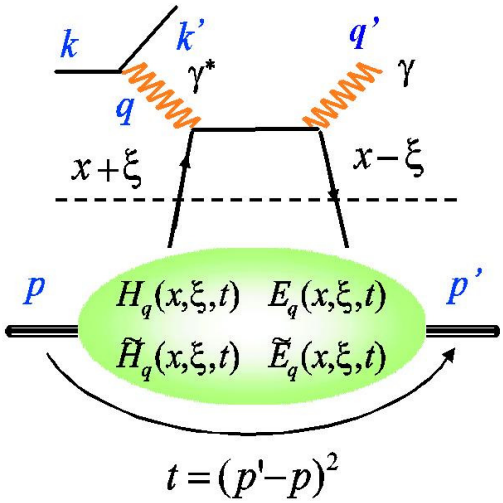

Figure 1: The handbag diagram for DVCS. An incident lepton of four-momentum k generates a virtual photon of four-momentum $q = k - k'$. The momentum four-vector of the scattered photon is q'. The initial and final momentum four-vectors of the nucleon are p and p' resulting in a total momentum transfer $t = (p' - p)^2 = (q - q')^2$. Additional (e, e') invariants are $y = q \cdot p/(k \cdot p)$, $W^2 = (q + p)^2$, $Q^2 = -q^2$, and $x_B = Q^2/(2q \cdot p)$. The GPD skewness invariant is $\xi = x_B/(2 - x_B)$.

Generalized parton distributions (GPDs) are a new theoretical tool, developed in the late 90s, which link form factors and parton distributions. They offer correlation information between the transverse location and the longitudinal momentum of partons and can access the contribution of the orbital angular momentum of quarks (and gluons) to the nucleon spin [1–3]. Deeply Virtual Compton Scattering (DVCS) on the nucleon is the simplest hard exclusive process involving GPDs. At leading twist, a virtual photon scatters on a single quark with a given longitudinal momentum fraction $x+\xi$. This quark becomes highly virtual and re-emits a real photon before coming back into the nucleon with a different longitudinal momentum $x-\xi$ (see Fig. 1). The amplitude to remove and restore the parton inside the nucleon is described, at the leading order in $1/Q$, in terms of four GPDs H, $\tilde{H}$, E and $\tilde{E}$ depending of the three variables x, ξ and the momentum transfer t. The GPDs appear in the DVCS amplitude under integrals over the variable x:

$$\begin{aligned} \mathcal{T}_{DVCS} &\propto \int_{-1}^{1} dx \left(\frac{1}{x-\xi+i\epsilon} \pm \frac{1}{x+\xi-i\epsilon} \right) GPD(x,\xi,t)\,, \\ &\propto P\int_{-1}^{1} dx \left(\frac{1}{x-\xi} \pm \frac{1}{x+\xi} \right) GPD(x,\xi,t) \; - i\pi \Big[GPD(\xi,\xi,t) \pm GPD(-\xi,\xi,t) \Big]\,. \end{aligned} \tag{1}$$

Experimentally DVCS interferes with the Bethe-Heitler (BH) process where the real photon is radiated by the incident or the scattered lepton (see Fig 2). In Hall A at Jefferson Lab, we measure both the polarized cross section difference with longitudinally polarized electrons and the unpolarized cross section. At leading twist:

$$\overrightarrow{\sigma} - \overleftarrow{\sigma} \sim 2 \cdot \Im m(\mathcal{T}^{BH} \cdot \mathcal{T}^{DVCS})\,, \tag{2}$$

$$\overrightarrow{\sigma} + \overleftarrow{\sigma} \sim \left|\mathcal{T}^{BH}\right|^2 + 2 \cdot \Re e(\mathcal{T}^{BH} \cdot \mathcal{T}^{DVCS}) + \left|\mathcal{T}^{DVCS}\right|^2. \tag{3}$$

Since the BH is purely real and fully calculable with the known form factors, the polarized cross section difference accesses the imaginary part of the DVCS amplitude and therefore a linear combination of GPDs at one point $x = \pm\xi$, while the unpolarized cross section accesses the real part of DVCS and therefore a linear combinations of GPD integrals over x (see Eq. 1). In addition, the unpolarized cross section allows to access the $\left|\mathcal{T}^{DVCS}\right|^2$ term which represents a bilinear combination of GPD integrals.

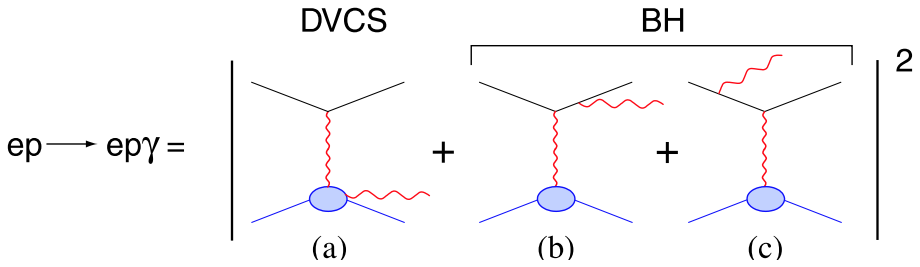

Figure 2: Lowest order QED diagrams for the process $eN \to eN\gamma$, including the DVCS (a) and the Bethe-Heitler (b, c) amplitudes.

To investigate neutron structure via electron scattering, a deuterium target frequently serves as a quasi-free neutron target because of the weak binding energy between the proton and the neutron inside the deuteron. Within the impulse approximation (IA), where only one nucleon is active and participates in the absorption and emission of the photon (the other nucleon being a spectator), the electroproduction of photons on a deuterium target may be decomposed into elastic (d-DVCS) and quasi-elastic (p-DVCS and n-DVCS) contributions:

$$\mathrm{D}(\vec{e}, e'\gamma)X = d(\vec{e}, e'\gamma)d + n(\vec{e}, e'\gamma)n + p(\vec{e}, e'\gamma)p + \ldots \tag{4}$$

Meson production channels also contributes background at large M_X^2. Therefore, with a deuterium target one can have three different DVCS processes: DVCS on the nucleon (p-DVCS and n-DVCS) and coherent DVCS on the deuteron (d-DVCS), which accesses deuteron GPDs [4–7]. Cross sections of n-DVCS (and d-DVCS) are then obtained from $\mathrm{D}(\vec{e}, e'\gamma)X$ events after subtraction of the proton quasi-elastic contribution deduced from measurements on a H_2 target.

Two experiments, dedicated respectively to p-DVCS and n-DVCS, ran in fall 2004 in Hall A. The p-DVCS experiment (E00-110) showed strong evidence of DVCS scaling for Q^2 as low as 2 GeV^2 [8]. This is a necessary step before interpreting the polarized cross-sections in terms of GPDs. We measured the first linear combinations of proton GPDs at three different Q^2 and at fixed x_B. These combinations are mainly sensitive to H and $\tilde{H}$. In the n-DVCS experiment (E03-106) we extracted, from the helicity-dependent cross section of $\mathrm{D}(\vec{e}, e'\gamma)X$ reaction on quasi-free neutrons off deuterium target, the same linear combination of GPDs, but with different weights (a consequence of the different neutron BH amplitude). The neutron helicity dependent cross section was mostly sensitive to $E(\pm\xi, \xi, t)$, the least constrained GPD [9]. The knowledge of E is essential because it enters on equal footing with H in Ji's sum rule leading to the total angular momentum carried by quarks in the nucleon [3]. In addition to providing different GPDs combinations, the neutron experiments have naturally a different flavor sensitivity to GPDs than the proton experiments and they appear as a mandatory step towards a better knowledge of the partonic structure of the nucleon. Figure 3 is a beautiful illustration of this complementarity between the neutron and the proton experiments.

Measurements of the unpolarized cross section are of great interest since they can access GPD integrals over x and therefore explore the regions $|x| \not\sim \xi$. Unfortunately, these measurements could not be done in E03-106. On the one hand, the interpretation of the unpolarized cross section in terms of GPD integrals requires the knowledge of the $\left|\mathcal{T}^{DVCS}\right|^2$ term in Eq. 3.

On the other hand, our measurement of the unpolarized cross section in E03-106 had very large systematic error bars ($\sim$50%). The latter is the consequence of:

- A large systematic error due to the uncertainty on the relative calibration between the H_2 and the D_2 data (almost one month separated the two data taking periods).
- A large systematic error due to the contamination of the DVCS-like channel $eD \to e'\pi^0 X \to e'\gamma X$. In fact, a high trigger threshold did not allow the recording of enough π^0 decays to properly evaluate this contamination.

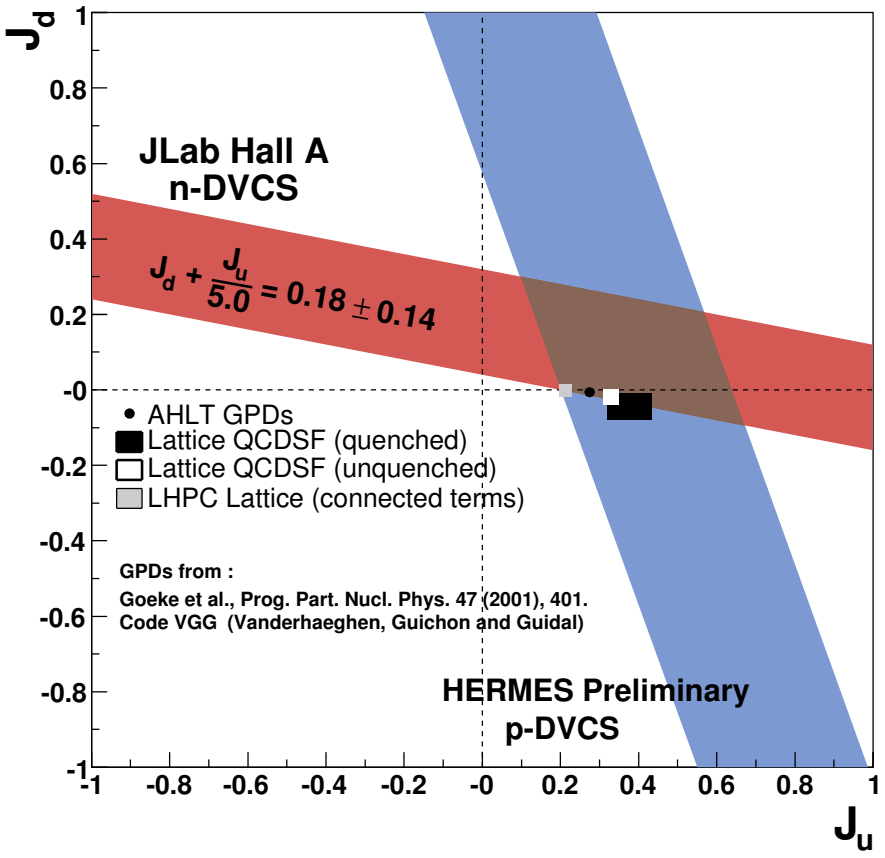

Figure 3: A model-dependent extraction of the contributions J_u and J_d of up- and down-quarks, respectively to the proton spin [9].

- The difficulty to separate the contribution on the coherent deuterium from the neutron

We propose in this experiment to measure DVCS observables off the neutron in parallel to the TDIS experiment. These combinations have naturally a different flavor sensitivity than the ones extracted from proton experiments. We will use exactly the same successful technique from the previous n-DVCS experiments where we detected only the scattered electron and the emitted photon. In our case, we will detect the electron with SBS, the photon with a existing high resolution electromagnetic calorimeter. The DVCS events are then identified with the missing mass technique and the n-DVCS (and possibly d-DVCS) will be associated with a spectator proton (or possibly a recoil deuton) will be detected in the TDIS TPC allowing to unambiguously discriminate an event on a neutron from an event on a proton (and possibly from a coherent event).

2 Deep photon electroproduction on the neutron

As shown in figure 2, both DVCS and BH processes contribute to the photon electroproduction cross section. In the differential phase space element $d^5\Phi = dQ^2 dx_{\rm B} dt d\phi_e d\phi_{\gamma\gamma}$, where ϕ_e is the azimuthal angle of the scattered electron and $\phi_{\gamma\gamma}$ is the angle between the leptonic and hadronic planes, the total cross section of photon electroproduction off an unpolarized target of mass M is given by [10]:

$$\begin{aligned}\frac{d^5\sigma(\lambda,\pm e)}{d^5\Phi} &= \frac{d\sigma_0}{dQ^2 dx_B}\left|\mathcal{T}^{BH}(\lambda)\pm\mathcal{T}^{DVCS}(\lambda)\right|^2\frac{1}{e^6}\\ &= \frac{\alpha^3_{QED}x_B y}{16\pi^2Q^2\sqrt{1+\epsilon^2_{DVCS}}}\left[\left|\mathcal{T}^{BH}(\lambda)\right|^2+\left|\mathcal{T}^{DVCS}(\lambda)\right|^2\mp\mathcal{I}(\lambda)\right]\frac{1}{e^6},\end{aligned} \tag{5}$$

where $\epsilon_{DVCS} = 2x_B M/Q$, λ is the electron helicity and the $\pm+$ stands for the sign of the charge of the lepton beam. Since the BH contribution is completely calculable in QED from the well known form factors at small $|t|$, a measurement of the polarized cross section will access the interference ($\mathcal{I}$) and the DVCS^2 ($\left|\mathcal{T}^{DVCS}\right|^2$) terms which depend respectively on a linear and a bilinear combination of GPD integrals. It is possible then to perform a $\phi_{\gamma\gamma}$ analysis in order to separate up to a certain degree the different contributions to the cross sections. At twist-3 accuracy [10]:

$$\mathcal{I}(\lambda) = \frac{e^6}{x_B y^3\mathcal{P}_1(\phi_{\gamma\gamma})\mathcal{P}_2(\phi_{\gamma\gamma})t}\left\{c_0^{\mathcal{I}}+\sum_{n=1}^{2}(-1)^n\left[c_n^{\mathcal{I}}(\lambda)\cos(n\phi_{\gamma\gamma})-\lambda s_n^{\mathcal{I}}\sin(n\phi_{\gamma\gamma})\right]\right\} \tag{6}$$

$$\left|\mathcal{T}^{DVCS}(\lambda)\right|^2 = \frac{e^6}{y^2Q^2}\Big\{c_0^{DVCS}-c_1^{DVCS}\cos(\phi_{\gamma\gamma})+\lambda s_1^{DVCS}\sin(\phi_{\gamma\gamma})\Big\}. \tag{7}$$

$\mathcal{P}_{1,2}$ are the electron propagators in the BH amplitude with a $\phi_{\gamma\gamma}$ dependence. In the previous equations, only the $\sin(n\phi_{\gamma\gamma})$ terms depend of the electron helicity. Consequently, the unpolarized cross section has a $\cos(n\phi_{\gamma\gamma})$ harmonic structure and the helicity-dependent cross section has a $\sin(n\phi_{\gamma\gamma})$ harmonic structure. It should be noticed that we have neglected the gluon tansversity terms, having a $(3\phi_{\gamma\gamma})$ weighting in Eq. 6 and a $\cos(2\phi_{\gamma\gamma})$ weighting in Eq. 7, because our measurements are in the valence quark region (x_B=0.36).

2.1 Interference terms

The Fourier coefficients $c_n^{\mathcal{I}}$ and $s_n^{\mathcal{I}}$ of the interference term (Eq. 6) are:

$$\begin{aligned}c_0^{\mathcal{I}} &= -8(2-y)\Re\mathrm{e}\left\{\frac{(2-y)^2}{1-y}K^2\mathcal{C}^{\mathcal{I}}(\mathcal{F})+\frac{t}{Q^2}(1-y)(1-x_B)\left[\mathcal{C}^{\mathcal{I}}+\Delta\mathcal{C}^{\mathcal{I}}\right](\mathcal{F})\right\}\\ \begin{Bmatrix}c_1^{\mathcal{I}}\\ \lambda s_1^{\mathcal{I}}\end{Bmatrix} &= -8K\begin{Bmatrix}(2-2y+y^2)\\ -\lambda y(2-y)\end{Bmatrix}\begin{Bmatrix}\Re\mathrm{e}\\ \Im\mathrm{m}\end{Bmatrix}\mathcal{C}^{\mathcal{I}}(\mathcal{F})\\ \begin{Bmatrix}c_2^{\mathcal{I}}\\ \lambda s_2^{\mathcal{I}}\end{Bmatrix} &= \frac{-16K^2}{2-x_B}\begin{Bmatrix}(2-y)\\ -\lambda y\end{Bmatrix}\begin{Bmatrix}\Re\mathrm{e}\\ \Im\mathrm{m}\end{Bmatrix}\mathcal{C}^{\mathcal{I}}(\mathcal{F}^{\rm eff}),\end{aligned} \tag{8}$$

where at the Bjorken limit

$$K^2 = \frac{t_{\rm min}-t}{Q^2}\left[1-x_B\right]\left[1-y\right]\left[1+\mathcal{O}(t/Q^2)\right]. \tag{9}$$

The $\mathcal{C}^{\mathcal{I}}$ and $\Delta\mathcal{C}^{\mathcal{I}}$ are the quantities to be extracted from the data and depend on the interference of the BH amplitude with the set $\mathcal{F} = \{\mathcal{H}, \mathcal{E}, \tilde{\mathcal{H}}\}$ of twist-2 Compton form factors (CFFs) or the related set $\mathcal{F}^{\rm eff}$ of effective twist-3 CFFs:

$$\mathcal{C}^I(\mathcal{F}) = F_1(t)\mathcal{H}(\xi,t)+\xi G_M(t)\tilde{\mathcal{H}}(\xi,t)-\frac{t}{4M^2}F_2(t)\mathcal{E}(\xi,t) \tag{10}$$

$$\mathcal{C}^I(\mathcal{F}^{\rm eff}) = F_1(t)\mathcal{H}^{\rm eff}(\xi,t)+\xi G_M(t)\tilde{\mathcal{H}}^{\rm eff}(\xi,t)-\frac{t}{4M^2}F_2(t)\mathcal{E}^{\rm eff}(\xi,t) \tag{11}$$

$$\left[\mathcal{C}^I+\Delta\mathcal{C}^I\right](\mathcal{F}) = F_1(t)\mathcal{H}(\xi,t)-\frac{t}{4M^2}F_2(t)\mathcal{E}(\xi,t)-\xi^2 G_M(t)\left[\mathcal{H}(\xi,t)+\mathcal{E}(\xi,t)\right], \tag{12}$$

where F_1 and F_2 are respectively the Dirac and Pauli form factors and $G_M = F_1 + F_2$. As mentioned above, $\mathcal{C}^{\mathcal{I}}(\mathcal{F}^{\rm eff})$ is a twist-3 term and has a $\sin(2\phi_{\gamma\gamma})$ or $\cos(2\phi_{\gamma\gamma})$ weighting. E00-110 results indicate that the contribution of this term to the polarized cross sections is small relatively to the twist-2 terms [8]. Therefore in E03-106, we have neglected the contribution of this term in our analysis. However, it would be exciting if it could generate a measurable signal.

The imaginary part of twist-2 CFFs is determined by the $x = \pm\xi$ points of the GPDs, whereas the real part is determined by a GPD integral over x. For example:

$$\mathcal{E}(\xi,t) = \sum_f e_f^2 \left\{ i\pi \Big[E_f(\xi,\xi,t) - E_f(-\xi,\xi,t) \Big] + \mathcal{P} \int_{-1}^{+1} dx \left[\frac{2x}{\xi^2 - x^2} \right] E_f(x,\xi,t) \right\} \quad (13)$$

$$\tilde{\mathcal{E}}(\xi,t) = \sum_f e_f^2 \left\{ i\pi \Big[\tilde{E}_f(\xi,\xi,t) + \tilde{E}_f(-\xi,\xi,t) \Big] + \mathcal{P} \int_{-1}^{+1} dx \left[\frac{2\xi}{\xi^2 - x^2} \right] \tilde{E}_f(x,\xi,t) \right\}, \quad (14)$$

where the sum $f \in \{u, d, s\}$ is over the flavor content of the nucleon, and e_f is the quark charge in unit of the elementary charge. From the previous equations, we can deduce that a measurement of the unpolarized cross section accesses the real part of CFFs and therefore a GPD integral over x, while a measurement of the helicity-dependent cross section probes the imaginary part of CFFs and therefore GPDs at $x = \pm\xi$.

2.2 Deuteron GPD Model Estimates

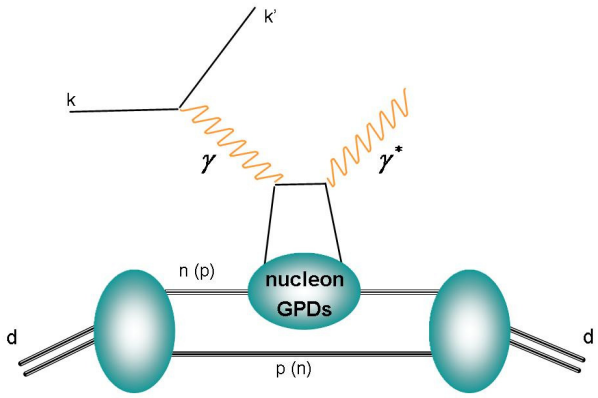

Figure 4: Coherent DVCS on the deuteron in the impulse approximation. The virtual photon interacts with a parton inside the nucleon, the other nucleon being spectator. Both nucleons recombine to re-form the deuteron in the final state.

Most of the models for the nucleon GPDs exploit the GPD relationship with form factors and parton distributions, supplemented with some assumptions about the ξ dependence. In the deuteron case, little is known experimentally about axial form factors or one of the parton distributions (b_1) which makes their parametrization difficult. In addition, four GPDs have vanishing first moments and then no information can be inferred about their t-dependence. To ride out these difficulties, the easiest way consists to use an impulse approximation where only one nucleon is active and participates in the absorption and emission of the photon (see Fig 4). The deuteron GPDs are then a convolution of the nucleon GPDs with the two-nucleon light-cone wave function of the deuteron [5,7]. In the model by F. Cano and B. Pire, only the nucleon GPDs H and $\widetilde{H}$ are considered since E and $\widetilde{E}$ go with suppressing kinematical prefactors [7] Figure 5 shows an estimate of the deuteron GPD combinations at 6 GeV kinematics (we could not get estimates for 11 GeV kinematics). According to this model, the $\mathcal{C}^{DVCS}$ term is, here also, at least 100 times bigger than the interference terms $\Re\mathrm{e}\left[\mathcal{C}^I\right]$ and $\Re\mathrm{e}\left[\mathcal{C}^I + \Delta\mathcal{C}^I\right]$. The rapid decrease as a function of $|t|$ is expected from the behavior of the deuteron form factors.

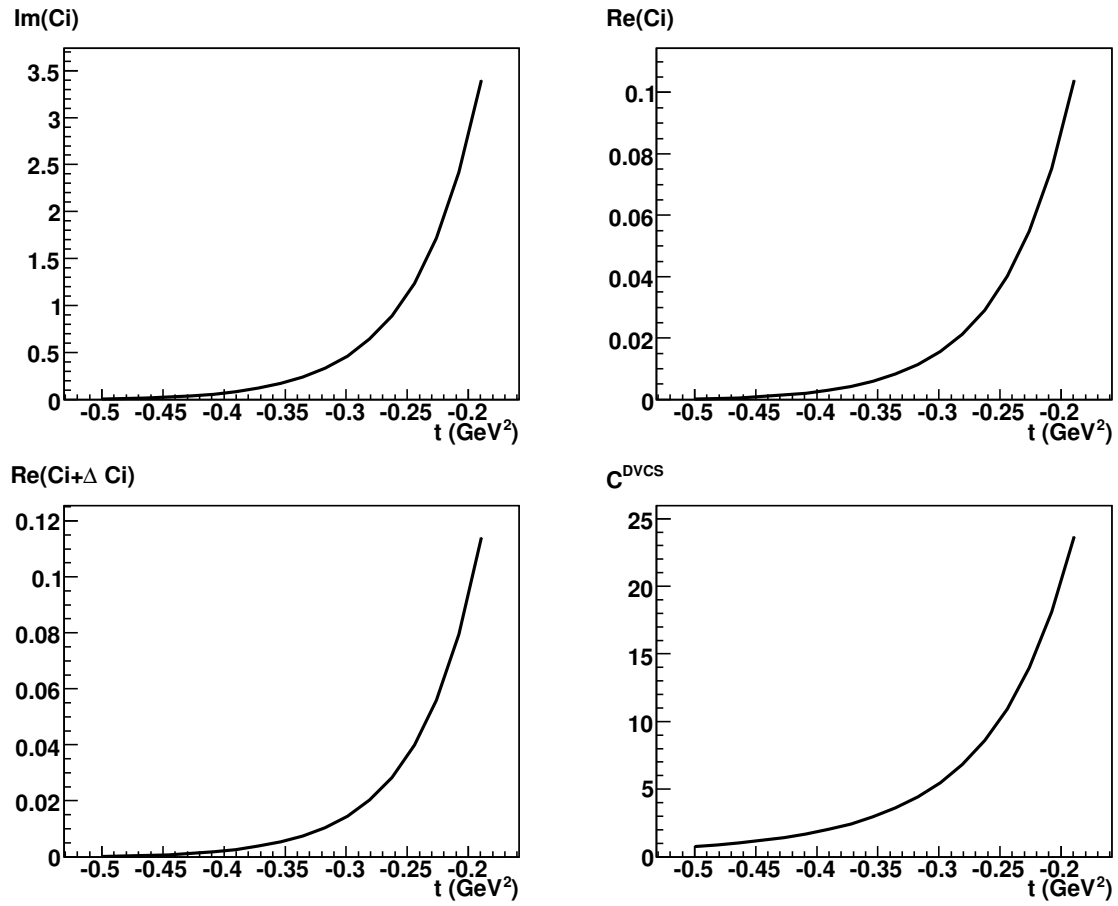

Figure 5: Calculation of the deuteron observables to be extracted from the data at our kinematics [7].

We have a hint that we will be able to detect the deuteron with our experimental apparatus (see section 7.2). We plan to provide a full study of the coherent d-DVCS with updated calculations of the model by F. Cano and B. Pire evaluated at 11 GeV for the next iteration of this proposal.

3 Deep π^0 electroproduction off the neutron (and deuteron)

The π^0 electroproduction longitudinal cross section provides an extremely interesting access to GPDs. Indeed, if the twist-2 contribution dominates the cross section, it provides a promising way to perform a flavor separation of GPDs. Moreover, π^0 production probes only the "polarized" GPDs in the nucleon ($\tilde{H}$ and $\tilde{E}$), which contain information about the spatial distribution of the quark spin. This complements DVCS measurements, where all GPDs participate.

At leading twist

$$\frac{d\sigma_L}{dt} = \frac{1}{2}\Gamma \sum_{h_N, h_{N'}} |\mathcal{M}^L(\lambda_M = 0, h'_N, h_N)|^2 \propto \frac{1}{Q^6} \qquad \frac{d\sigma_T}{dt} \propto \frac{1}{Q^8} \tag{15}$$

with

$$\mathcal{M}^L \propto \left[\int_0^1 dz \frac{\phi_\pi(z)}{z}\right] \int_{-1}^1 dx \left[\frac{1}{x-\xi} + \frac{1}{x+\xi}\right] \left\{\Gamma_1 \widetilde{H}_{\pi^0} + \Gamma_2 \widetilde{E}_{\pi^0}\right\}(x,\xi,t) \tag{16}$$

The Γ factors in Eq. (15) and Eq. (16) are kinematics factors and ϕ_π is the pion distribution amplitude. The

flavor combination of GPDs entering in Eq. (16) is different from that in DVCS on the nucleon. Indeed,

$$|\pi^0\rangle = \frac{1}{\sqrt{2}}\{|u\bar{u}\rangle - |d\bar{d}\rangle\} \qquad \widetilde{H}_{\pi^0} = \frac{1}{\sqrt{2}}\left\{\frac{2}{3}\widetilde{H}^u + \frac{1}{3}\widetilde{H}^d\right\}, \tag{17}$$

whereas in DVCS on the proton and neutron:

$$\begin{aligned} |p\rangle &= |uud\rangle, \qquad H^{(p)}_{DVCS} = \frac{4}{9}H^u + \frac{1}{9}H^d\,, \\ |n\rangle &= |udd\rangle, \qquad H^{(n)}_{DVCS} = \frac{1}{9}H^u + \frac{4}{9}H^d\,. \end{aligned} \tag{18}$$

In the neutron case, we have applied isospin symmetry, and defined the flavor GPDs $H^{u,d}$ in terms of the proton flavor contributions.

As in the case of the DVCS unpolarized cross section, with these measurements we access a GPD integral over x. Note that at twist-2 level, the pion distribution amplitude $\phi_\pi(z)$ enters only as a normalization integral. Note also that the amplitude of Eq. (16) enters squared in the cross section. Therefore, a bilinear combination of these GPD integrals are measured.

The differential π^0 electroproduction cross section reads:

$$\frac{d\sigma}{dt} = \frac{d\sigma_T}{dt} + \epsilon\frac{d\sigma_L}{dt} + \sqrt{2\epsilon(1+\epsilon)}\frac{d\sigma_{LT}}{dt}\cos\phi + \epsilon\frac{d\sigma_{TT}}{dt}\cos 2\phi + \lambda\sqrt{2\epsilon(1-\epsilon)}\frac{d\sigma_{LT'}}{dt}\sin\phi \tag{19}$$

where λ is the electron helicity and where the virtual photon polarization is given by:

$$\epsilon = \left(1 + 2\frac{|\mathbf{q}|^2}{Q^2}\tan^2\frac{\theta}{2}\right)^{-1}. \tag{20}$$

Along with DVCS cross sections, DVCS experiments at Jefferson Lab have also measured the exclusive π^0 electroproduction cross section off the proton [11–13] and the neutron [14] in the deep inelastic regime. Similarly to DVCS, an extraction of the neutral pion electroproduction cross section with spectator proton identification will greatly reduce the systematic uncertainty due to the proton/neutron separation. We plan to perform this measurement as well, as it would come "for free" with the DVCS measurement. However, we have not been able to provide an estimation of the neutral pion electroproduction statistics expected from this experiment, and plan to provide it for the next iteration of this proposal.

4 Proton-neutron event separation with mTPC

The biggest advantage of performing this measurement with the mTPC is the unambiguous identification of the deep exclusive γ and π^0 events off the neutron (and potentially off the deuteron, although we would still need to determine that fact), thanks to the detection and measurement of the spectator proton. Plus, the measurement of the spectator proton provides information on the struck neutron, which allows to partially cancel the missing mass broadening due to the Fermi motion (see Fig. 25 in section 7.3).

Previous neutron experiments in Hall A [9, 14] have relied on the subtraction of the proton event yield $\mathrm{H}(e,e'\gamma)X$ or $\mathrm{H}(e,e'\pi^0)X$ from the total deuteron yield $\mathrm{D}(e,e'\gamma)X$ or $\mathrm{D}(e,e'\pi^0)X$. Such subtraction leads to an increased systematic uncertainty. Figs. 6 and 7 show the missing mass spectra, respectively for exclusive γ and π^0 production, off the deuteron and off the proton normalized at the same luminosity, and the result of the subtraction of the latter from the former, with their respective statistical errors. One may remark the size of the error bars on the $D-H$ yield difference (blue asterisks on Fig. 6, hollow squares on Fig. 7). These errors end up driving the systematic uncertainties on the results made available by these publications.

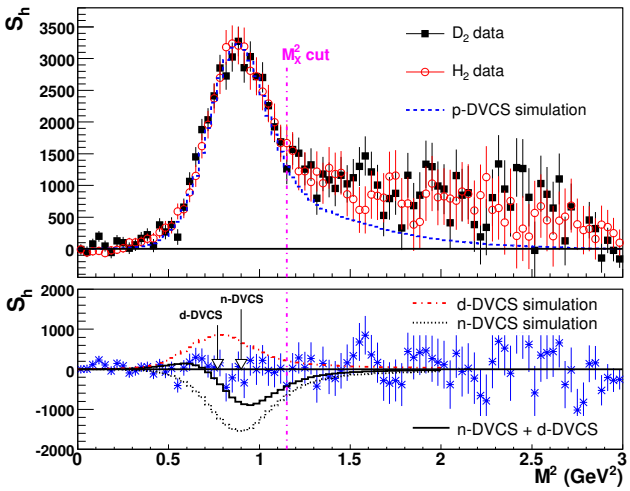

Figure 6: Missing mass distributions for exclusive γ production from [9]. (top) Helicity signal $S_h = \int_0^{\pi}(N^+ - N^-)\,d^5\Phi - \int_{\pi}^{2\pi}(N^+ - N^-)\,d^5\Phi$ for $\mathrm{D}(e,e'\gamma)X$ and $\mathrm{H}(e,e'\gamma)X$ events; H_2 data are folded with a momentum distribution of the proton in deuterium, and scaled to the D_2 data luminosity; the simulation curve is for the Fermi broadened $\mathrm{H}(e,e'\gamma)p$ reaction. (bottom) Residual helicity signal after H_2 subtraction; the arrows indicate the M_X^2 average position of n-DVCS and d-DVCS events for $< t >= -0.3$ GeV^2; the simulation curves, integrated over the complete experimental acceptance and obtained for the arbitrary values $\Im\mathrm{m}\left[\mathcal{C}_n^I\right]^{exp} = -\Im\mathrm{m}\left[\mathcal{C}_d^I\right]^{exp} = -1$, illustrate the sensitivity of the data to the neutron and deuteron signals.

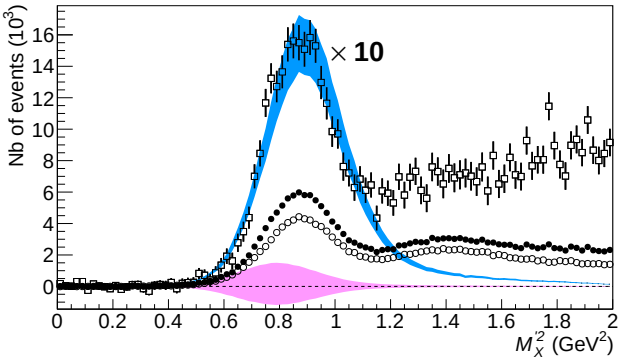

Figure 7: Missing mass distributions for exclusive π^0 production from [14]. Corrected missing mass squared $M_X'^2$ for $\mathrm{D}(e,e'\pi^0)X$ (solid circles) and normalized Fermi-smeared $\mathrm{H}(e,e'\pi^0)X$ events (open circles). Bars show statistical uncertainties. The difference between the two distributions (squares) is scaled by a factor 10 for clarity. The blue and magenta bands (both scaled $\times 10$), show the simulated $n(e,e'\pi^0)n$ and $d(e,e'\pi^0)d$ yields, respectively, fit to the data by minimizing $\chi^2 = \sum_{i=1}^{3600}\left(\frac{N_i^{exp} - N_i^{sim}}{\delta_i^{exp}}\right)^2$. These bands include the statistical uncertainty of the fit.

5 Experimental setup

5.1 Overview

We propose to measure the exclusive photon and neutral pion electroproduction on deuterium, with identification of the spectator proton $D(e, e'\gamma p_{\rm spec})n$ and $D(e, e'\pi^0 p_{\rm spec})n$, in the valence region ($x > 0.1$) and deep inelastic regime ($Q^2 > 1$ GeV^2, $W^2 > 2GeV^2$).

The key to this experimental technique is to measure the very low-energy outgoing spectator proton, in triple coincidence with the deeply inelastically scattered electron and the high energy photon (or pair of high energy photons in the π^0 case).

The analysis of double coincidence events $D(e, e'\gamma)n$, together with $H(e, e'\gamma)p$, to extract Deeply Virtual Compton Scattering (DVCS) cross sections on the neutron (by subtraction of DVCS on hydrogen from the total exclusive photon production off deuterium) has already proved successful [9], albeit with large systematic uncertainties on the estimation of $n(e, e'\gamma)n$.

The identification of the DVCS events off the neutron can be obtained with the measurement of the recoil neutron, as it has been proposed by [15], or with the identification of the spectator proton, which is the measurement we propose in this document, and which has also been proposed by ALERT [16]. The latter technique has the advantage over the former that the spectator proton momentum and vertex can be measured with significantly better precision (if not with significantly better efficiency) than the recoil neutron. Plus, it gives an handle on the Fermi momentum of the struck neutron. Both effects greatly reduce the systematic uncertainties.

Our experiment proposes to perform our measurement *using the already approved Tagged Deep Inelastic Scattering experiment (TDIS) [17] in Hall A with the Super BigBite Spectrometer,* **with no other modification that the addition of an electromagnetic calorimeter for high energy photon detection.** The TDIS experiment will employ the Super BigBite Spectrometer (SBS) to detect the scattered electrons, in time and vertex coincidence with low momentum proton(s) measured in a low radiation length radial modular Time Projection Chamber (mTPC). Our measurement will use the exact same setup, with the addition of a calorimeter to detect the high energy photon. A representation of this setup is shown on Fig. 8. As for the TDIS experiment, SBS will be located at 12 degrees on the right side of the beam, and the mTPC

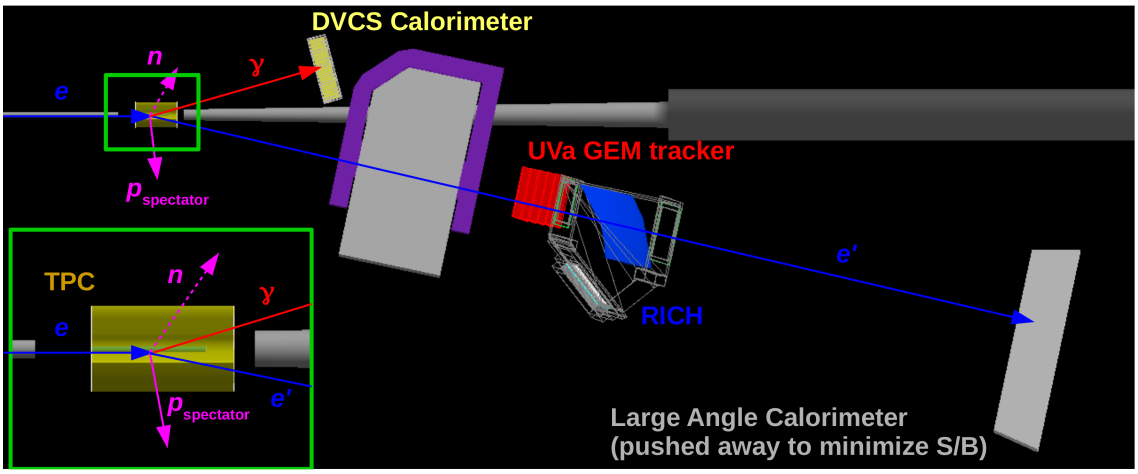

Figure 8: Geant4 model of the experimental setup for the proposed experiment.

will be located around the target. The calorimeter will be located at 14.85 degrees on the left side of the beam.

5.2 Experiment Luminosity

The proposed measurement concerns a process with a relatively low cross section (typically fractions of nb), which requires a relatively high luminosity and/or wide acceptance to collect a significant statistics. In

addition to this, the detection efficiency of the very low momentum spectator proton will provide a significant reduction of the available statistics. (Note that a n-DVCS experiment including neutron recoil detection will have a similar drop of statistics due to the neutron detector efficiency). Besides, the spectator tagging technique requires a relatively low density target to reduce the detection threshold of the spectator, which limits the intensity.

ALERT [16], which will run in Hall B, will benefit from the 2π azimuthal coverage of the CEBAF Large Acceptance Spectrometer upgrade at 12 GeV (CLAS 12); however, the maximal beam intensity in Hall B is intrinsically limited to ~ 200 nA, their luminosity will be relatively low ($10^{35}\,\mathrm{cm}^{-2}\mathrm{s}^{-1}$)

The Super BigBite Spectrometer has an acceptance of ~ 30 msr, which is obviously relatively modest compared to the CLAS12 instrument. However, Hall A could receive much higher beam intensities, and TDIS plans to use up to 50 to 60 μA .

5.2.1 Target cell

The TDIS/n-DVCS target will consist in a 40 cm long, 1 cm diameter straw filled with gaseous deuterium (or hydrogen), at 6.4×10^{-4} g/cm^{-3} In order to minimize the energy loss of the protons of interest, we have reduced the material of the target wall as much as possible, down to 20 micrometers of Kapton. To achieve the target density, one could either use a gas at room temperature and $\sim$4 atm, or a gas at 90 K and 1.2 atm. The choice will ultimately depend on the pressure the walls are able to handle (or by how much they need to be thickened). Combined with the beam intensity, this will provide us an instant luminosity per nucleon of $3.0 \times 10^{36}\,\mathrm{cm}^{-2}\mathrm{s}^{-1}$.

5.3 TDIS setup: SBS and mTPC

As stated previously, *for our experiment we use the standard, already approved, TDIS setup with no other modification than the addition of an electromagnetic calorimeter*. This section is dedicated to the description of this TDIS setup. A more extensive description of this setup is available in the TDIS proposal [17], namely for details about the SBS data acquisition.

Super Big Bite Spectrometer in TDIS setup: overview The Super BigBite Spectrometer (SBS) is a ~ 30 msr acceptance spectrometer, composed of a single dipole magnet and a modular detector package. It has been mainly (but not exclusively) dedicated to Form Factors measurements at high Q^2 ([18–20]). In these experiments (and others such as SIDIS [21]), SBS will be used as the "hadron arm", to detect the hadronic final state (recoil nucleon), and is being instrumented accordingly: an hadronic calorimeter, and additional detectors: "CDet" hodoscope (G_M^n), GEM equipped focal plane polarimeter (G_E^p), etc. SIDIS requires an additional RICH detector for hadron identification, and 5 planes of GEM trackers, each made of four modules of 60×50 cm^2, arranged to form 60×200 cm^2 trackers. n-DVCS (and TDIS), will be one of the very few SBS experiments using it in "electron mode", which requires a slightly different detector package. This detector package includes most of the SBS detector package for SIDIS (including GEM trackers and RICH), but substituting the hadronic calorimeter for one module of the CLAS Large Angle Calorimeter (LAC), and modifying the RICH for electron/pion separation. The following three sub subsections describe the detector systems that are specific to the Super BigBite spectrometer in electron mode. Please note that these modifications are necessary for TDIS.

CLAS6 Large Acceptance Calorimeter The conceptual drawing of the internal structure of the LAC is shown in Fig. 9. The LAC module has a rectangular shape with a sensitive area of 217 x 400 cm^2 and consists 33 layers, each composed of a 0.20 cm thick lead foil and 1.5 cm thick NE110A plastic scintillator bars. The total thickness is about 12.9 radiation lengths or 1 hadronic absorption length. Each scintillator layer is protected from contact with the lead by 0.02 cm thick Teflon foils. The width of the scintillators is roughly 10 cm and is slightly increasing from the inner layers toward the outer layers to provide a focusing geometry. Scintillators in consecutive layers are rotated by 90 degrees to form a 40 x 24 matrix of cells with area approximately 10 x 10 cm^2. The module is vertically divided into two groups: an inner (first 17 layers) and an outer (16 layers) groups. Each group has its own light readouts. Scintillators lying one on top of the other with the same orientation form a stack. For each stack the light is collected at both ends separately

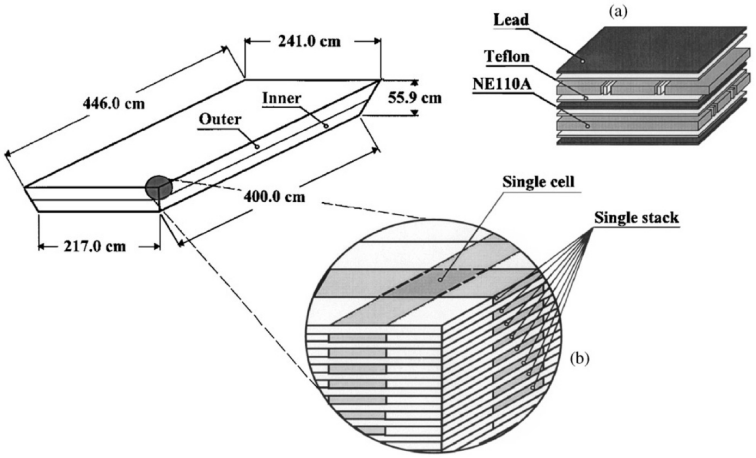

Figure 9: The conceptual drawing of the internal structure of the LAC module.

using light guides coupled to EMI 9954A photomultiplier tubes. For each module there are 128 stacks and 256 photomultipliers [22].

The LAC energy resolution for electromagnetic showers is 7.5 ± 0.2 % [22]. Combined with CLAS, the pion contamination is less than 1% for cuts that give a detection efficiency of 95% for 2 GeV electrons.

The performance of this equipment for pion rejection has been evaluated with Monte Carlo for the TDIS proposal, and one may refer to [17] for more details about this matter.

Ring Imaging Cherenkov The RICH (Ring Imaging CHerenkov) has been recovered from the HERMES experiment at DESY [23]. Its original purpose (which will be the same for SIDIS) was to identify pions, kaons and protons, over a wide momentum range (to 12 GeV/c or above from ∼0.5 GeV/c for π/K, and from ∼2 GeV/c for K/p), from the reconstructed Cherenkov rings generated while the particles go through the radiator media. The RICH indeed bears two Cherenkov radiators: an array of aerogel tiles ($n = 1.03$) covering the RICH aperture, for identification at lower particle momentum, and a heavy radiator gas (C_4F_{10}, $n = 1.00137$), for identification at higher momentum. The Cherenkov light rings are reflected by a spherical mirror to a large array of 1938 2.5 cm diameter XP1911 PMTs (see Fig.10).

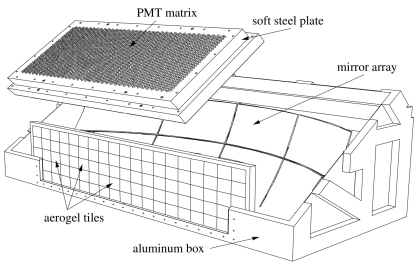

Figure 10: the HERMES RICH detector [23]. In electron mode, the aerogel tiles will be removed; the gas might also be substituted for lighter gas.

In TDIS/n-DVCS, the RICH can be modified for the purpose of electron identification and pion rejection. First, the aerogel tiles can be removed entirely to suppress any low momentum signal apart from electrons. Second, the radiator gas, C_4F_{10}, can be substituted for lighter gas with a lower index of refraction (e.g. CO_2, CF_4), which increases even further the pion threshold, while still providing a sufficient signal for the RICH.

5.3.1 mTPC concept

The mTPC (for "multiple/modular Time Projection Chamber") is a 55 cm long time projection chamber with a cylindrical geometry, centered on and surrounding the 40 cm target. Its purpose is the detection of the low energy spectator protons for the TDIS measurements, or the spectator proton in n-DVCS on deuterium, all being within the range of 50 to 350-400 MeV/c. Fig 11 shows a drawing of this detector.

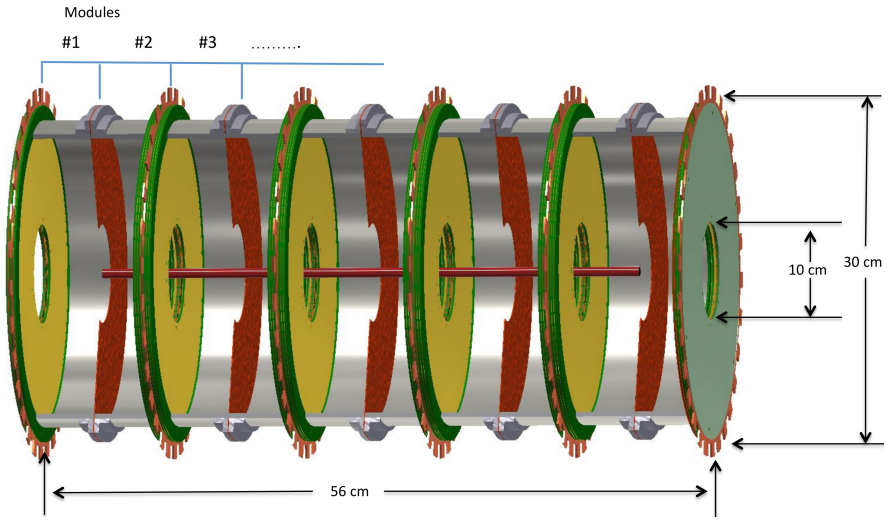

Figure 11: mTPC current design. It is composed of 10 sub-modules of 5 cm each, to minimize the drift time in each module and allow for a faster detector response. The yellow disks are the readout planes.

Its main feature is its longitudinal segmentation, which is capital provided the experiment luminosity and background. Extensive Monte-Carlo simulation work carried out by the TDIS collaboration within the GEANT-4 simulation framework has indicated that the background rates at the TPC detector location will be as high as 670 MHz; this is significantly higher than the rates handled in similar size TPCs before. Dividing the detector not only reduces significantly the background received in each segment, but it also allows to minimize the drift time. This combined with other design features (e.g. drift electric field parallel to the solenoidal magnetic field) allows this instrument to achieve a maximum drift time of the order of 1-2 μs (reduction by a factor 20-40 with respect to other designs.

The drifting electrons from the ionizing particle will be amplified and detected by Gas Electron Multiplier (GEM) foil based readout disks. The TPC drift volume readout (the yellow disks on Fig 11) consists of two GEM layers, each mounted on a 2 mm thick holding frame, followed by a readout surface containing conducting pads connected to readout electronics through traces on the back of the readout and then through a flex circuit strip. Each readout pad will have an area of 5 x 5 mm^2 separated by gaps of 100 μm, yielding approximately 2500 pads per readout. This arrangement gives position resolution of approximately 1.5 mm. The drift gas will be composed of 90% ^{4}He and 10% CH_4. This choice is dictated by the necessity to have a low Z material to minimize the number of secondaries created in the gas, and is made at the expense of an increased drift time.

The proposed modular design allows the mTPC to handle high background rates, at the cost of reduced efficiency and reduced momentum resolution due to the presence of readout disks in the middle of the active area which reduce the track lengths in the drift volume. Any track reconstructed in the mTPC with a momentum uncertainty of over 10% is rejected, leading to decreased efficiency. This is our current definition of mTPC efficiency for both the TDIS and the n-DVCS experiment. A semi-empirical map of the mTPC efficiency as a function of the proton momentum and angle (with respect to the beam direction) is shown on (Fig 12). The efficiency in the range of 50% to 70% for detecting proton tracks with momenta in the range of 50 MeV/c to 300 MeV/c with a transverse momentum resolution of 10% or better. For tracks in the momentum range of 300 MeV/c to 400 MeV/c, this efficiency is higher than 20%. Note that the mTPC has azimuthal symmetry with the current simulated geometry, so there is no phi dependence on the efficiency. These available inefficiencies are sufficient to meet the physics goals of the TDIS program and of the n-DVCS

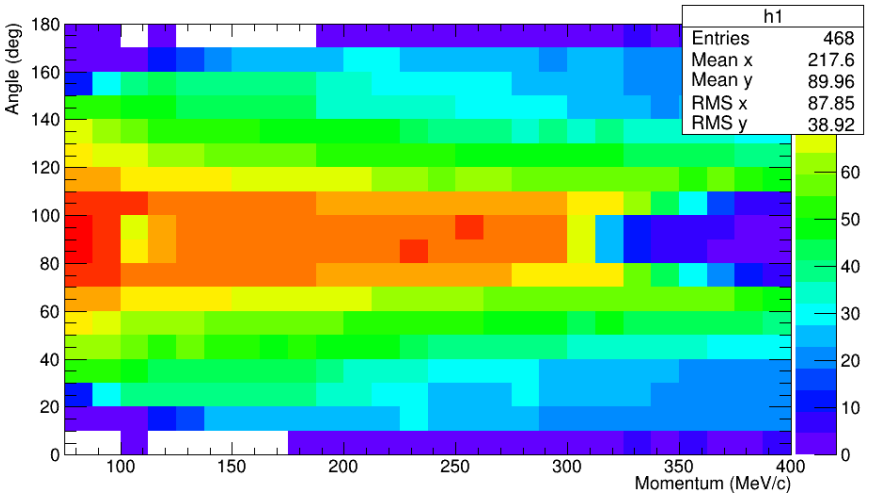

Figure 12: mTPC efficiency.

program. For instance, we determined with our Monte Carlo simulations of $en \to en\gamma$ on deuterium that the global efficiency for the detection of n-DVCS events with spectator proton association is $\sim$25 %.

5.4 DVCS calorimeter

The high energy photon will be measured by a dedicated electromagnetic calorimeter. Again, this calorimeter is the only specific equipment that we require to perform the n-DVCS measurement in addition to the TDIS setup. Our primary option for this detector is the calorimeter from the Neutral Particle Spectrometer [24].

The basic concept for the NPS is a highly segmented electromagnetic calorimeter preceded by a compact sweeping magnet. The experiments it enables, require detection of neutral particles with energies ranging between 0.5-7.6 GeV with good energy resolution (1-2%), and good coordinate (2-3 mm) and angular resolution of 0.5-0.75 mrad.

The NPS will consist of an array of up to 1116 scintillating $PbWO_4$, possibly combined with up to 208 PbF_2 crystals. Both types of crystals are fast ($PbWO_4$: 5-14 ns and PbF_2: $<$ 30ns) and so suitable for the experiments, which require fast signals with short tails to minimize pile-up at high rates, e.g., timing resolution of better than 100 ns. In general, the NPS needs crystals with high transparency, high light yield, good timing where 90 % of the light is emitted within 30-50 ns, and good radiation hardness. NPS will likely take advantage of the existing $PbWO_4$ crystals of the high-resolution inner part of the Hybrid Electromagnetic Calorimeter (HYCAL) [25, 26] used for PRIMEX /PRIMEX-II experiments.

Our plan is to use the same $PbWO_4$ crystals NPS will use *without the sweeping magnet*. The crystals would be arranged similarly to the PRIMEX calorimeter, within 31 row and 36 columns, as shown on Fig. 13. The main drawback to this option is the potential unavailability of the NPS calorimeter $PbWO_4$ blocks. Our backup option in this case is to use the PbF_2 blocks from the Hall A DVCS calorimeter. The main disadvantage of this second option is a broader resolution both in energy (due to the lower light yield for these blocks) and in position (due to the larger transverse size of the blocks). Another disadvantage is the relatively compact size of this calorimeter which does not offer sufficient spatial coverage, but this can be easily overcome with the addition of other calorimeter blocks, for instance the lead glass blocks from the SBS G_E^p electromagnetic calorimeter [20].

The calorimeter would be located around 2 m away from the target, at a fairly close angle from the beamline (14.85 degrees). This configuration maximizes our counting rates, but exposes the calorimeter to the SBS magnetic fringe field. For this reason, the blocks will need to be readout by either silicon PMTs (Si-PM) or Avalanche Photo-Diodes (APDs). Many options nowadays exist for relatively large area APDs such as used by the HPS experiment in Hall B or for 6×6 mm^2 multi-pixel photon counter S13360-6075PE by Hamamatsu. The best option for the DVCS calorimeter readout still needs to be studied thoroughly.

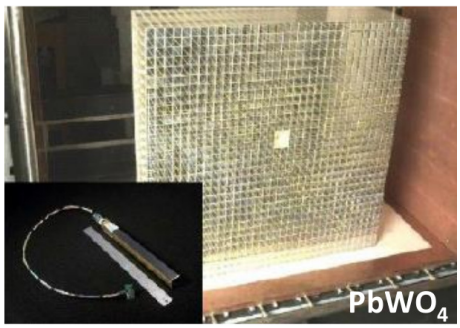

Figure 13: Inner part of the PrimEx calorimeter, composed of 1116 PbWO4 blocks. NPS will use a slightly different layout, but we plan to arrange these in a similar fashion as PRIMEX.

The readout will be done using JLab FADC 250, this allows to continuously send the calorimeter data to a trigger module computing sums of adjacent 5x5 matrix of blocks. The calorimeter will be readout if one sum is above threshold of 1.5 GeV. To reduce the data, only FADC channels part of the cluster will be transferred.

6 Beam Induced Background

A Geant4 simulation was used to study beam induced background rates, primarily in the DVCS calorimeter, due to its close position to the target. An initial electron beam, of energy 11 GeV was generated, incident upon a 40 cm length, 1.905 cm diameter, D_2 target, held at 1 atm.

The estimated rates $R_{Background}$ were calculated as:

$$R_{Background} = N \times \frac{I_{Beam}}{q_e \times N_{Generated}}, \tag{21}$$

where N, I_{Beam}, q_e and $N_{Generated}$ are respectively: the number of hits recorded in the detector; the beam current ($50\,\mu$A), the elementary electron charge (in units C); the initial number of generated events. The simulations were performed using statistics of $N_{Generated} = 99.1 \times 10^9$ events.

As expected the rate per block decreases rapidly with energy threshold as shown in Fig. 14.

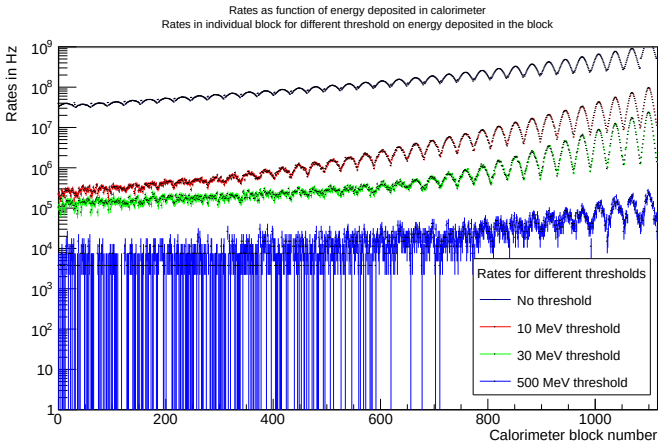

Figure 14: Rates in individual calorimeter blocks for different thresholds

Rates drop quickly over the surface of the calorimeter and are dominated by the blocks close to the beamline with single rates up to 20 MHz level with a 30 MeV threshold as shown in Fig. 15.

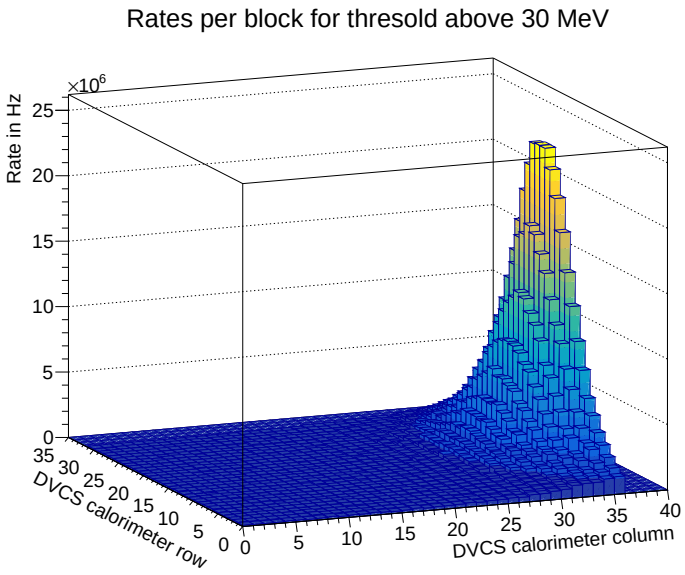

Figure 15: Rates in individual calorimeter blocks for a 30 MeV threshold and as a function of position in the calorimeter

In order to reduce the data from low energy background, we will be using a feature of the FADC readout, allowing to compute sums of 3x3 blocks and only readout the group of 9 blocks which are above threshold.

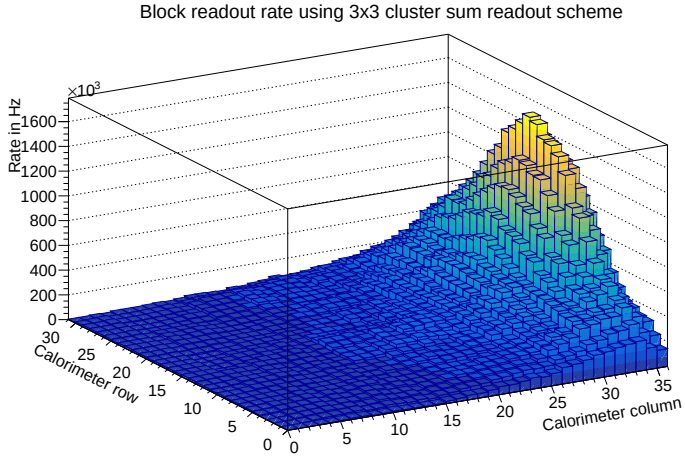

Figure 16: Rates in individual calorimeter blocks for a 1.5 GeV threshold on 3x3 cluster sum and as a function of position in the calorimeter

This further reduces the rate of highest rates blocks readout down to a few MHz (Fig. 16) for the highest rate block. We assume we readout 25 samples for a 100 ns windows. Those blocks will be readout for most trigger. By using the same fitting technique as for DVCS timing resolution will be reduced down to 1 ns which will reject most accidentals from the hot blocks.

Average number of blocks is 24 (Fig. 17), assuming 25 samples readout (100 ns) this give an event size of 12 (headers) + 10*2*24 = 1200 bytes. At the expected trigger rate of TDIS of 6 KHz, this gives a data rate of 7.2 MB/s which will be negligible compared to the amount of the TPC data.

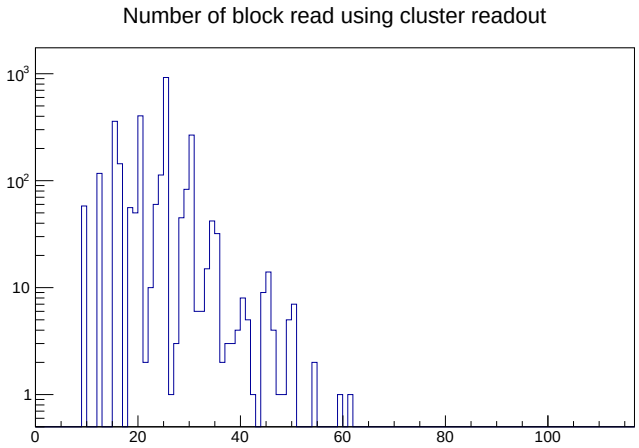

Figure 17: Typical numbers of blocks readout using the cluster readout scheme for clusters above 1.5 GeV

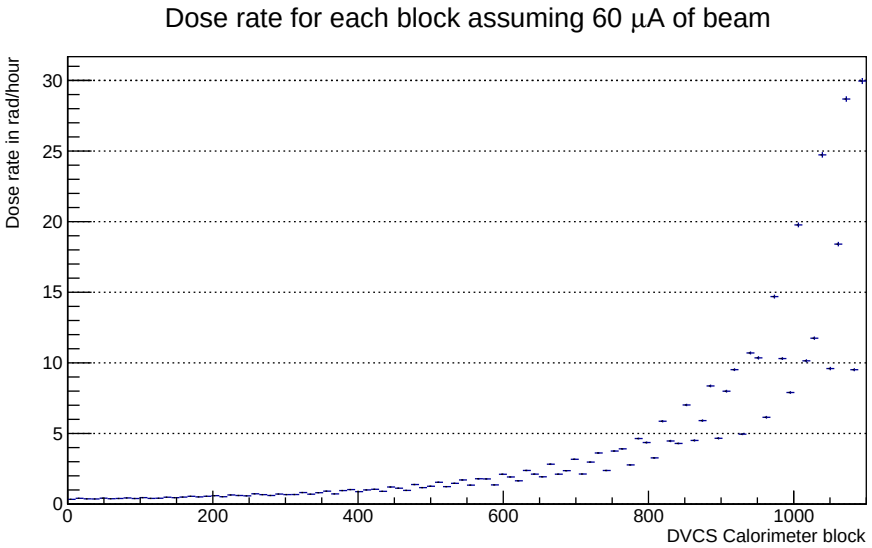

Figure 18: Dose rate in the calorimeter block for 60 μA on Deuterium at 1 atm in rad per hour

By weighting the block hits by the energy deposit one can determine the dose rate in each calorimeter block (Fig. 18).

The maximum dose rate for the block the closest from the beam line is 30 rad per hour. The total dose rate for 600 hours of beam is thus 18 krad, which is reasonable since the threshold for annealing of the calorimeter is 50 krad of integrated dose.

We conclude that given the radiation dose and occupancies of the calorimeter, adding the calorimeter to the TDIS setup is a viable solution. Further reduction of rate will be obtained after more careful background studies.

7 Analysis Technique

The data analysis will share similarities with the one performed in E03-106 [9], namely for the extraction of the DVCS observables, described in section 7.4). The main difference will be that the detection of the

spectator proton will allow an unambiguous identification of n-DVCS events. This, however, makes our extraction very dependent of the mTPC calibration, described in section 7.0.1.

We do, however, have the possibility to extract useful physics results relatively quickly with the extraction of n-DVCS beam spin asymmetry $A_{\rm LU}$ (the first subscript translating a longitudinally polarized beam, the second subscript U translating an unpolarized target), which writes as:

$$A_{\rm LU} = \frac{N_+ - N_-}{N_+ + N_-} \tag{22}$$

where N_+ (resp. N_-) is the event yield for beam longitudinal helicity + (resp. -). Note that measuring this beam spin asymmetry requires the measurement of the beam polarization which relies, in Hall A, on two types of measurements:

- dedicated Møller polarimeter measurements (typically 4 hours each). For the duration of this experiment, two measurements should be sufficient.
- continuous Compton polarimeter measurements, which can be taken simultaneously with the production data.

Our analysis will also rely on a careful calibration of the calorimeter, which is described described in section 7.1.

7.0.1 mTPC Calibration

The proposed measurement of the tagged DIS cross section will require good knowledge of the various detector acceptances and efficiencies. The fully inclusive electron-proton and electron-deuteron cross sections are well known from experiments in this kinematic regime at Jefferson Lab and SLAC [27]. Comparing our untagged DIS measurements with these data will allow for precision checks of the acceptance, efficiency, and other corrections used for the SBS electron spectrometer analysis.

The mTPC will also require study and calibration. The full calibration method is described in details in the TDIS proposal [17], but let us summarize here the basic idea. The mTPC calibration will be achieved by the combination of two channels:

- the measurement of proton tracks from elastic electron-proton scattering which can be distinguished from the TDIS protons of interest, as they will be preferentially be peaked perpendicular to the beam to be in the same momentum range.
- the quasi-elastic electron scattering from the deuteron for the mTPC calibration. The energy and direction of the spectator proton may be determined in this reaction reaction measuring the scattered electron in the SBS in combination with a neutron measured with the (relocated) SBS Hadron Calorimeter (HCAL), which will not be required otherwise for TDIS.

This last measurement would require the specific setup described on Fig. 19 and would run for 24 hours at 4.4 GeV bean energy and reduced luminosity of 0.3×10^{36} Hz/cm^2, granting more than 6 million events of tagged protons for the study of the mTPC.

7.1 Calorimeter Calibration

Our goal is to have many calibration methods to calibrate the calorimeter. Usually, in Hall A DVCS experiments, the DVCS calorimeter was calibrated via the elastic H$(e, e'p)$ reaction, with the proton measured in the spectrometer (in our case it would be SBS), and the electron measured in the calorimeter. This calibration also serves to check the geometrical surveys of the calorimeter and the spectrometer. However, this calibration requires setting changes, which would constrain us to either request additional beam time including setting changes.

We have studied the possibility to perform this elastic calibration within an existing setting of the experiment, but the existing settings lead to extremely low elastic rates, which could not allow us to perform a calibration with the optimal accuracy (ideally 1 %, and not worse than $\sim$3 %). This constrains us to request

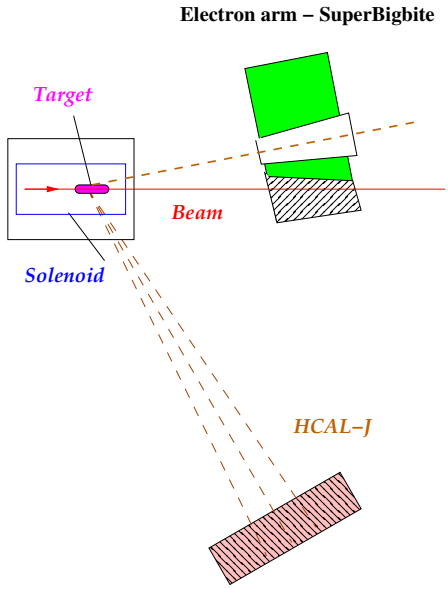

Figure 19: Setup for mTPC calibration. SBS will be located at the same angle of 12 degrees, and HCAL at 60 degrees and 15 meters distance from target.

additional beam time for a change of setting involving a move of SBS. This operation by itself is expected to take 24h. We have thought of a preliminary setup and plan for the elastic calibration on hydrogen and shall be able to achieve it within 24 hours beam time. In this setup (also available on Fig 20, SBS will be located at an angle of 50 degrees, and as close as possible from the target (1.5 m, or even 1 m if possible). The calorimeter will be located at 14.85 degrees and 4 meters away from the target.

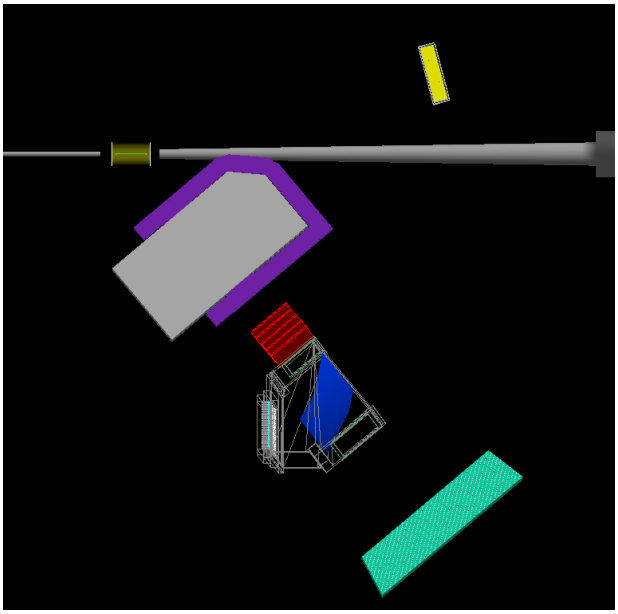

Figure 20: Geant4 model of the proposed setup for elastic calibration. This setup would require moving the Super BigBite spectrometer from 12 degrees and 2.5 m to 50 degrees and 1 m, and the calorimeter from 2 m to 4 m.

While in the setting the elastic electron cover only one half of the calorimeter (see Fig 21), we could

imagine a smart setup (like setting the calorimeter on a platform sliding on rails) to shift the calorimeter by the required amount (36 cm stop-to-stop) in a fast, efficient, and reliable way, and collect the statistics for the other half of the calorimeter, and perform the full calorimeter calibration at a 3% accuracy within 24 hours of beam. Again, this plan is still preliminary and the setup itself could be optimized further. This

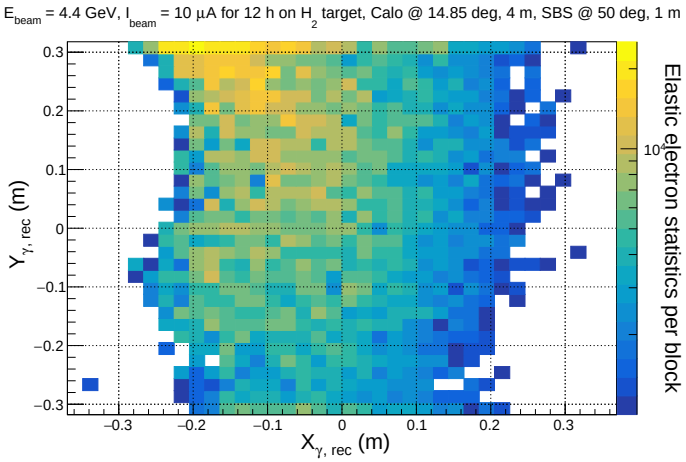

Figure 21: Estimated counts of elastic electrons in each block of the DVCS calorimeter obtained within 12 hours of beam at 0.3×10^{36} Hz/cm^2 with the setting described in the text. Slightly more than one half of the calorimeter is covered by the elastic electrons and gather the minimum required statistics of 1000 events within those conditions, which will allow to calibrate the full calorimeter within 24 hours beam time.).

calibration will be fully sorted out for the next iteration of this proposal.

For the calorimeter continuous monitoring during the experiment, we also have a calibration method relying on the reconstructed π^0 mass with two detected photons in the calorimeter. The comparison between the pion mass and the position of the invariant mass peak (Fig. 22 left) for different regions in the calorimeter allows us to identify miscalibrated blocks.

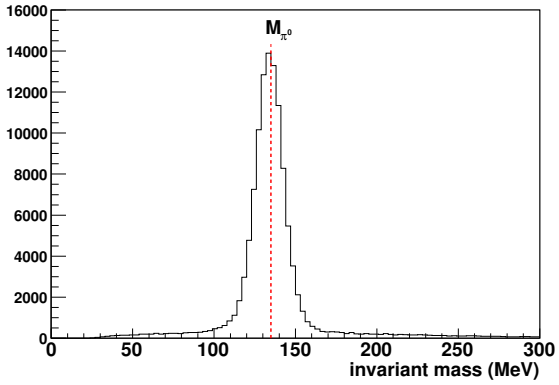

Figure 22: invariant mass of two detected photons in the calorimeter; the peak corresponds to photons coming from symmetric π^0 decays in the lab frame.

7.2 The Impulse Approximation

The data analysis will share similarities with the one performed in E03-106 [9], namely for the extraction of the DVCS observables, described in section 7.4). The main difference will be that the detection of the spectator proton will allow an unambiguous identification of n-DVCS events. This, however, makes

our extraction very dependent of the mTPC calibration, described in section 7.0.1. Since the momentum transfer to the recoil DVCS nucleon is large compared the momentum distribution of the nucleons inside the deuteron, we expect the DVCS reaction to be well described by the impulse approximation (IA), where the virtual photon scatters on a quasi-free nucleon, the other one acting as a spectator. Fig. 23 shows the Fermi momentum distribution together with the momentum distribution of the DVCS recoil particle in the proposed kinematics. The overlap between these distributions is less than 3%. This means the plane wave description of the final state is orthogonal to the bound deuteron, making final state interaction effects between a pn pair small. Thus, the inclusive yield on a deuterium target can be expressed as:

$$\begin{aligned} \mathrm{D}(\vec{e},e'\gamma)X &= d(\vec{e},e'\gamma)d + n(\vec{e},e'\gamma)n + p(\vec{e},e'\gamma)p + \ldots \\ &= \text{d-DVCS} + \text{n-DVCS} + \text{p-DVCS} + \ldots \end{aligned} \tag{23}$$

where the "..." denotes meson production channels.

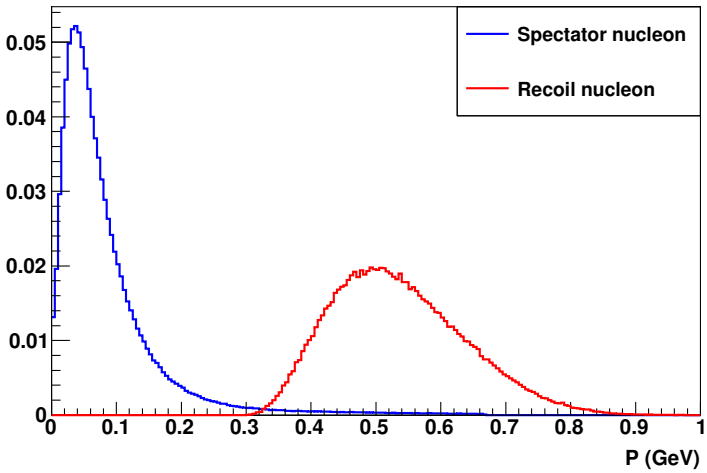

Figure 23: Normalized momentum distributions of the spectator proton (blue) in the deuteron (Fermi momentum distribution) and the n-DVCS recoil neutron (red) in the proposed kinematics. The overlap between these distributions is less than 3%.

Our experimental setup (section 5) has the potential to detect deuterons from low momenta. Fig. 24 shows that the detection threshold for deuterons will be below 100 MeV/c.

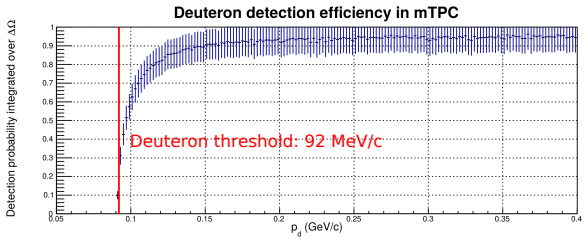

Figure 24: Deuteron detection probability at low momentum (between 0.05 and 0.2 GeV/c). Our target and mTPC design (see section 5) will allow deuteron detection starting from 92 MeV/c.

7.3 Selection of n-DVCS events

We propose to detect our DVCS sample on the neutron in triple coincidence $D(e,e'\gamma p_{spec})n$, the scattered electron being detected by the SBS, the photon by the calorimeter, and the spectator proton p_{spec} by the

mTPC.

The requirements for the three detected particles are the following:

- The scattered electron should pass through all five GEM plans, leave a significant signal in the RICH (at least 4 photoelectrons), and deposit at least 0.5 GeV in the LAC (which corresponds to a 1.5 GeV electron); In addition, we request that the virtual photon-nucleon CMS energy W is above 2 GeV, and that the virtual photon reconstructed from the electron is centered in the inner quarter of the calorimeter (see Fig 25).

- The photon is selected with a cluster in the DVCS calorimeter with an energy of at least 1 GeV and the reconstructed cluster position cannot be located in one of the peripheral, most outer blocks (see again Fig 25);

- The spectator proton is required to be detected by the TPC volume, and to be reconstructed with a resolution of 10 %.

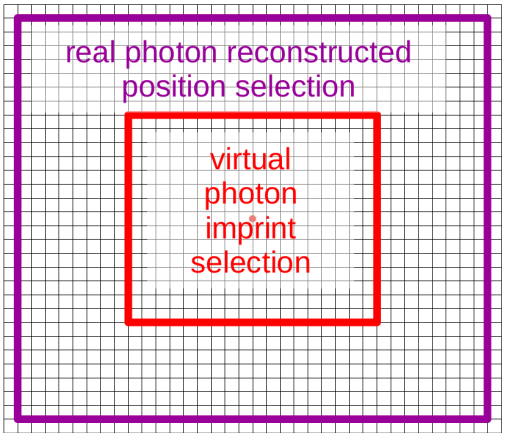

Figure 25: Selection of the virtual photon imprint (red) and the real photon reconstructed position (magenta) projected on the calorimeter surface.

The missing mass is reconstructed with the help of the spectator proton:

$$M_X^2 = (k + n_{FM} - k' - q')^2 \tag{24}$$

with k, k', 4-vectors of incident and scattered electron, 4-vector of initial neutron, q', 4-vector of produced photon, and n_{FM}, the 4-vector of the initial neutron *inferred from the detected spectator proton* p_{spec} ($\vec{n}_{FM} = -\vec{p}_{spec}$, within the assumption of the impulse approximation). Fig. 26 shows the effect of the inclusion of the spectator proton information on the missing mass resolution, from $\sim$0.16 (GeV/c^2)^2 without (red, blue on Fig. 26) to $\sim$0.11 (GeV/c^2)^2 with (green on Fig. 26). This constitutes a dramatic improvement. The value of the missing mass squared will provide an additional selection criterion for the selection of exclusive events: we require that the missing mass squared M_X^2 is below the pion production threshold $(M_N + m_\pi)^2 = 1.15(GeV/c^2)^2$ Note that in the case of the coherent DVCS on the deuterium (d-DVCS), one could apply a similar selection, except we would associate the $D(e, e'\gamma)X$ events with a recoil deuteron (which can be discriminated from spectator proton thanks to their twice as high signal amplitude/momentum ratio).

7.4 Extraction of DVCS observables

The extraction of the DVCS observables is based on the Belitsky-Kirchner-Mueller formalism of the cross sections [6, 10]. After the selection of n-DVCS events as described above, we write the experimental cross

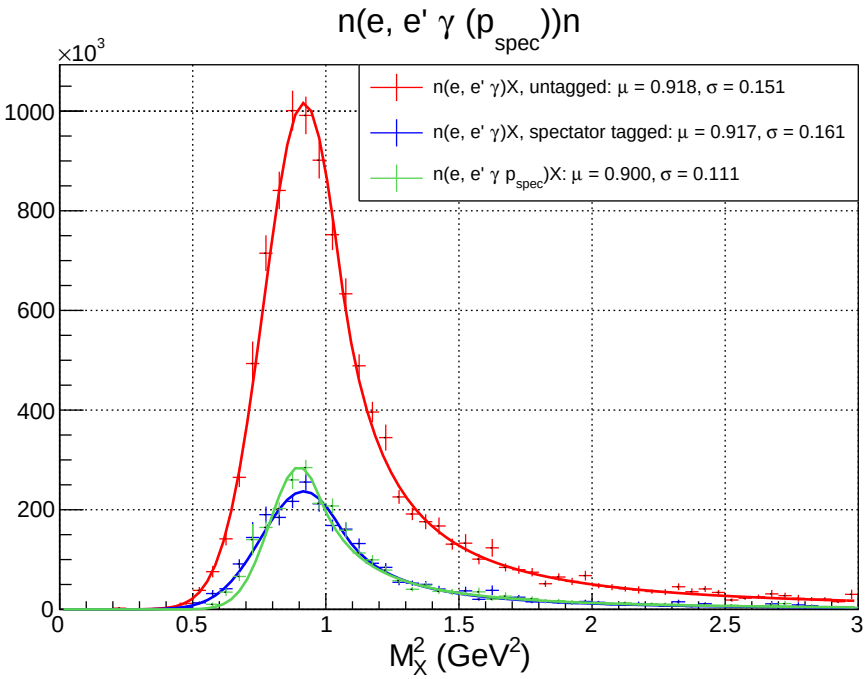

Figure 26: Effect of the detection and inclusion of the spectator proton in the reconstructed missing mass squared spectrum. Red: reconstructed missing mass squared for all n-DVCS events (including those not associated with a spectator proton - hence, not using its information); Blue: reconstructed missing mass squared for n-DVCS events with an associated spectator proton, but not using the spectator proton info in the missing mass; Green: reconstructed missing mass squared for n-DVCS events using the spectator proton information.

section as

$$\frac{d^5\sigma_n}{d^5\Phi} = \frac{d^5\sigma(|BH|^2_n)}{d^5\Phi} \tag{25}$$

$$+ \quad \Gamma_n^{DVCS}\,\mathcal{C}_n^{DVCS} + \frac{1}{\mathcal{P}_1\mathcal{P}_2}\left(\{\Gamma^{\Re}_{0,n} - \cos(\phi_{\gamma\gamma})\Gamma^{\Re}_{1,n}\}\Re\mathrm{e}\left[\mathcal{C}_n^I\right] + \Gamma^{\Re}_{0,\Delta,n}\Re\mathrm{e}\left[\mathcal{C}_n^I + \Delta\mathcal{C}_n^I\right]\right) \tag{26}$$

Six observables will be fit for each t bin (highlighted in red in Eq. 25). We minimize:

$$\chi^2 = \sum_i \left[\left(Y_i^{\mathrm{Exp}} - Y_i^{\mathrm{Fit}}\right)^2/\sigma_i^2\right]. \tag{27}$$

The Y_i^{Exp} are the experimental yields, after accidental and π^0 subtractions, in bin i, with statistical errors σ_i. The fit yields, $Y_i^{\mathrm{Fit}} = \sum_\Gamma \mathcal{C}_\Gamma K_\Gamma(i)$, depend linearly on the fitting harmonics $\mathcal{C}_\Gamma$ and the Monte-Carlo integrated kinematic weights:

$$K_\Gamma(i) = \mathcal{L}\sum_{j=1}^{N^{\mathrm{sim}}}\frac{\Delta^3\Phi_e\Delta^2\Phi_\gamma(j)}{N^{\mathrm{sim}}}\Gamma_\Gamma(j)\eta(i,j). \tag{28}$$

$\mathcal{L}$ is the integrated experimental luminosity and N^{sim} is the total number of events in the simulation. The phase-space factors are $\Delta^3\Phi_e = \Delta Q^2\Delta x_{\mathrm{Bj}}\Delta\phi_e$ and $\Delta^2\Phi_\gamma = 2\pi[t_{\mathrm{min}}(Q^2, x_{\mathrm{Bj}}) - t_{\mathrm{max}}]$. The indicator function $\eta(i,j) = 1$ if simulation event j lands in experimental bin i, otherwise, $\eta(i,j) = 0$.

The simulation takes into account the detectors acceptance and resolution and it includes both external and real internal radiative effects. Virtual radiative corrections will be applied as a correction factor to each

experimental bin (depending on $\phi_{\gamma\gamma}$ and t), following recent work by P.A.M. Guichon, based on [28] using a GPD model [29] for the VCS amplitude. These corrections differ at most 2% bin-to-bin relative to the global radiative corrections previously applied.

The binning is performed on 4 experimental variables :

- The $\phi_{\gamma\gamma}$ angle, in order to separate the $\cos(\phi_{\gamma\gamma})$ contributions in Eq. 25.
- The transfer t, in order to study the t-dependence of the extracted coefficients.
- The photon virtuality Q^2, in order to study the $Q2$-dependence of the extracted coefficients at similar values of x_{Bj}.
- The DIS quark "momentum" x_{Bj}.

8 Kinematics and additional time request

We propose to run simultaneously with the TDIS experiment in Hall A [17]. Table 1 summarizes the physics

Luminosity	
Beam current	25 μA
Target (density)	D_2, (6.5×10^{-4} g cm^{-3})
Ldt	1.5×10^{36} cm^{-2} s^{-2} per neutron
Super BigBite Spectrometer setup	
Angle	12 degrees
Distance from target	2.5 m
$\int Bdl$	-0.90 T m
$\Delta\Omega$	60 msr
Calorimeter	
Angle	14.85 degrees
Distance from target	2.0 m
$\Delta\Omega$	120 msr

Table 1: n-DVCS (and TDIS) physics data taking setup.

data taking settings for this experiment. Thanks to the relatively large SBS acceptance, our single setting allows us to collect a wide kinematic coverage in the valence region, which can then be subdivided into many kinematics. We have divided our acceptance into 3 main regions:

- "low" $x_{Bj} < 0.30$
- intermediate $0.3 < x_{Bj} < 0.42$
- large $x_{Bj} > 0.42$

Fig 27 shows the kinematic coverage and proposed binning for our $n(e, e'\gamma p_{spec})n$ sample in the deep inelastic regime ($W > 2$ GeV). Note this binning was meant to split about evenly the statistics between each x_{Bj}, Q^2 bin, and is certainly susceptible to evolve.

We have summarized the TDIS beam time request in table 2, which includes 10 days production on hydrogen, 5 days production on deuterium, and time request for calibrations and systematic studies. The n-DVCS experiment proposes to take production data during the 5 days of running on deuterium, at a total luminosity of 3×10^{36} cm^{-2} s^{-1} (1.5×10^{36} cm^{-2} s^{-1} on the neutron).We have added to this table a *tentative* preliminary beam time request specific to n-DVCS. This additional time represent 10 % of the beam time already requested by TDIS, and will be dedicated to the two following goals:

- perform the calorimeter calibration (see section 7.1), which will require a movement of the SBS. This operation itself requires 24 hours of down time. Fortunately, for the short duration of the n-DVCS

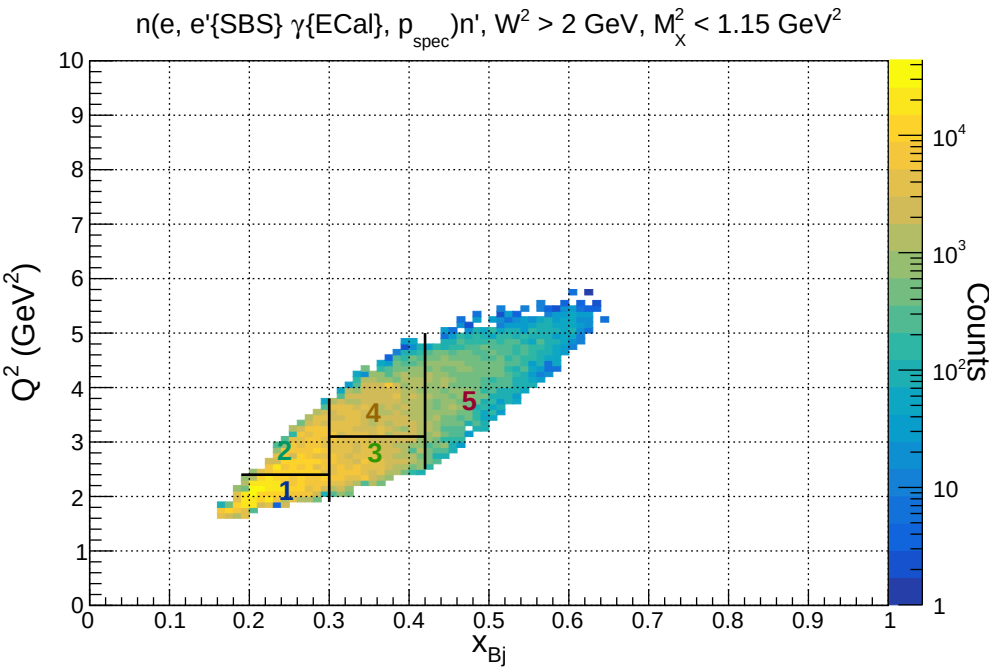

Figure 27: Q^2 vs x_{Bj} kinematic coverage of our $n(e,e'\gamma p_{spec})n$ sample in the deep inelastic regime ($W >$ 2 GeV), including selection on electron, virtual and real photon, and association with spectator proton coverage.

data taking, one calibration (hence one spectrometer move) should suffice, provided that we could also rely on the π^0 calibration, which will allow to monitor the calibration continuously. The calibration itself will take 24 hours beam time.

- perform a few (2-3 maximum) Møller measurement(s) for the beam polarization measurement, to extract the beam helicity dependent DVCS observables. This measurement will also be completed with the continuous measurement of the beam polarization with the Hall A Compton polarimeter. Such measurements, though not required for TDIS, shall not affect the quality of their data.

TDIS existing beam time request				
Target	Current (μA)	Beam Energy (GeV)	Beam Time (hrs)	Notes
Hydrogen	50	11	264	includes 1 day for commissioning
Deuterium	25	11	144	includes 1 day for commissioning
Hydrogen	5	11	120	
Deuterium	5	4.4	16	mTPC calibration with HCAL
			8	Beam Energy Changes
Total (TDIS)			552	23 days
Preliminary additional beam time request for n-DVCS				
			24	SBS move
Hydrogen	6	4.4	24	DVCS calorimeter calibration
			12	Møller measurements
Total (n-DVCS only)			60	2.5 days
Total (TDIS + nDVCS)			612	25.5 days

Table 2: Summary beam time request for the TDIS experiment, as described in the TDIS proposal [17], to which we added our tentative additional beam time request, motivated in the text.

9 Projected results

In order to compute the projected exclusive photon electroproduction rates on the neutron (and the proton), we used a Monte Carlo simulation including the response of detectors in GEANT4, weighted with the VGG program [30] including the Bethe Heitler and the DVCS cross sections; these yields are then normalized with the experiment luminosity indicated with Tab 1. Our total expected $en \to en\gamma$ statistics statistics is roughly about 9×10^5 events The statistics is summarized bin-by-bin in table 3. The average statistical accuracy for each bin in ϕ ranges from 1 % at lower Q^2, x_{Bj}, t to $\sim$5 % at the highest Q^2, x_{Bj}, t. Table 4 lists the expected systematics uncertainties for TDIS, completed with the expected systematics uncertainties specific to DVCS. The global systematic uncertainty expected from the n-DVCS measurement totals less than 8 %.

We have also projected the beam spin asymmetries as a function of ϕ for the neutron for a few selected x_{Bj}, Q^2 bins in Figs 28, 29 and 30 (corresponding respectively to bins 1, 3, and 5 on Fig. 27). The n-DVCS beam spin asymmetries (estimated with VGG) are modest at low t but become somewhat sizable at higher t (up to $\geq$0.1 at lower x_{Bj}, Q^2, or $\geq$0.05 at higher x_{Bj}, Q^2). One may observe a fair agreement between these data and our projection, which provides us some confidence in our simulation. These projections show that we would be able to perform a measurement of the DVCS channel on the neutron with a good statistical accuracy on a fairly extended x_{Bj} (from $\sim$0.2 to $\sim$0.5) and Q^2 coverage (from $\sim$2.0 to $\sim$4.0 GeV^2), with a relatively modest amount of beam time. We are also interested to measure $en \to en\pi^0$ process, as well as coherent exclusive processes on deuterium $ed \to ed\gamma$ and $ed \to ed\pi^0$. Complete estimations of expected yields for these processes will be done for the next iteration of this proposal.

$\|t\|$ bin	$en \to en\gamma$ events	statistical uncertainty per ϕ bin	$ep \to en\gamma$ events	statistical uncertainty per ϕ bin
	$x_{Bj} < 0.30$			
	$Q^2 < 2.4GeV^2$		$Q^2 > 2.4GeV^2$	
$0.0 < \|t\|(GeV^2) < 0.2$	164.0 10^3	1.0 %	90.1 10^3	1.3 %
$0.2 < \|t\|(GeV^2) < 0.5$	129.0 10^3	1.1 %	105.0 10^3	1.2 %
$0.5 < \|t\|(GeV^2) < 0.8$	22.5 10^3	2.7 %	21.4 10^3	2.7 %
$0.8 < \|t\|(GeV^2) < 1.2$	6.6 10^3	4.9 %	8.6 10^3	4.3 %
	$0.30 < x_{Bj} < 0.42$			
	$Q^2 < 3.1GeV^2$		$Q^2 > 3.1GeV^2$	
$0.0 < \|t\|(GeV^2) < 0.2$	26.9 10^3	2.4 %	19.5 10^3	2.8 %
$0.2 < \|t\|(GeV^2) < 0.5$	87.9 10^3	1.3 %	79.0 10^3	1.4 %
$0.5 < \|t\|(GeV^2) < 0.8$	21.6 10^3	2.7 %	29.3 10^3	2.3 %
$0.8 < \|t\|(GeV^2) < 1.2$	10.1 10^3	4.0 %	13.2 10^3	4.8 %
	$x_{Bj} > 0.42$			
$0.2 < \|t\|(GeV^2) < 0.5$	17.5 10^3	3.0 %		
$0.5 < \|t\|(GeV^2) < 0.8$	17.9 10^3	3.0 %		
$0.8 < \|t\|(GeV^2) < 1.2$	11.3 10^3	3.8 %		
$1.2 < \|t\|(GeV^2) < 2.0$	5.9 10^3	5.2 %		
Total counts	887 10^3			

Table 3: Estimated counts for $en \to en\gamma$ and $ep \to ep\gamma$ events for each x_{Bj}, Q^2 bin. The $en \to en\gamma$ events have been considered within the selection defined in section 7.3; The $ep \to en\gamma$-DVCS events have been considered within a similar selection, except for not requiring a spectator proton detected in the mTPC.

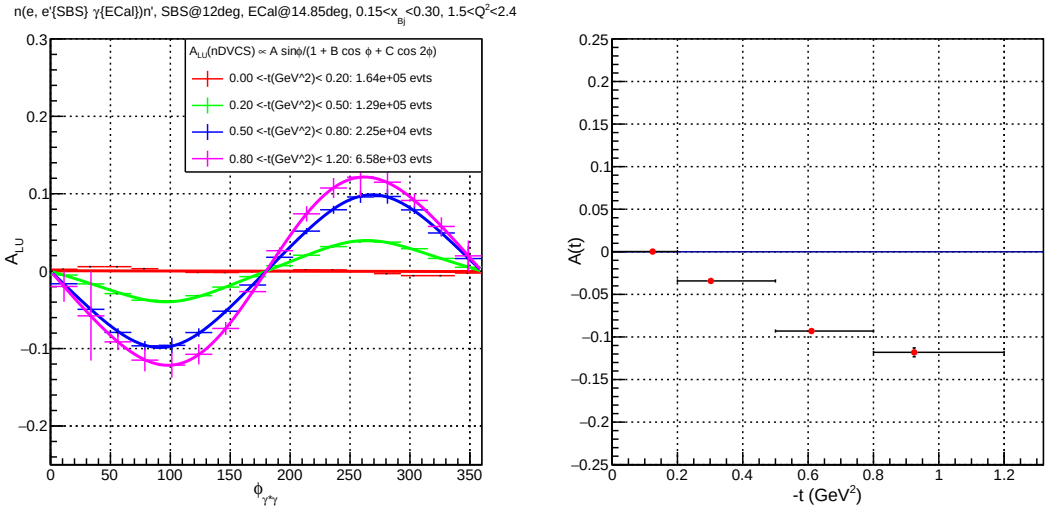

Figure 28: Projected DVCS beam spin asymmetry for the neutron as a function of $\phi_{\gamma\gamma}$ (left panel) and fitted $sin\phi$ component A as a function of t (right panel) for our lower x_{Bj}, Q^2 bin (bin 1 on Fig. 27). The statistics for each t bin is indicated in the legend.

Source	Uncertainty
TDIS	
Accidental background subtraction	5%
DIS electron cross section (Targ. density, beam charge, acceptance, det. efficiency)	3%
mTPC absolute efficiency	2%
mTPC deadtime	1%
mTPC momentum resolution	$< 1\%$
mTPC angular acceptance	1%
Beam position	$< 1\%$
Total TDIS	6.5 %
n-DVCS	
beam polarization	2%
π^0 subtraction	2%
e(p,e'γ)πN contamination	2%
radiative corrections	2%
Total n-DVCS	7.6 %

Table 4: Summary of systematic uncertainties for TDIS and n-DVCS.

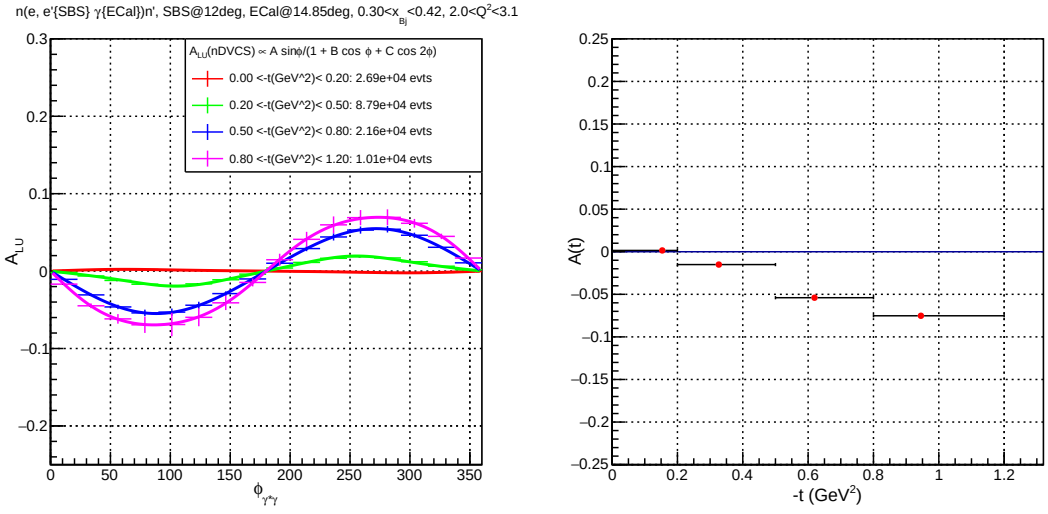

Figure 29: Projected DVCS beam spin asymmetry for the neutron as a function of $\phi_{\gamma\gamma}$ (left panel) and fitted $sin\phi$ component A as a function of t (right panel) for our intermediate x_{Bj}, lower Q^2 bin (bin 1 on Fig. 27). The statistics for each t bin is indicated in the legend.

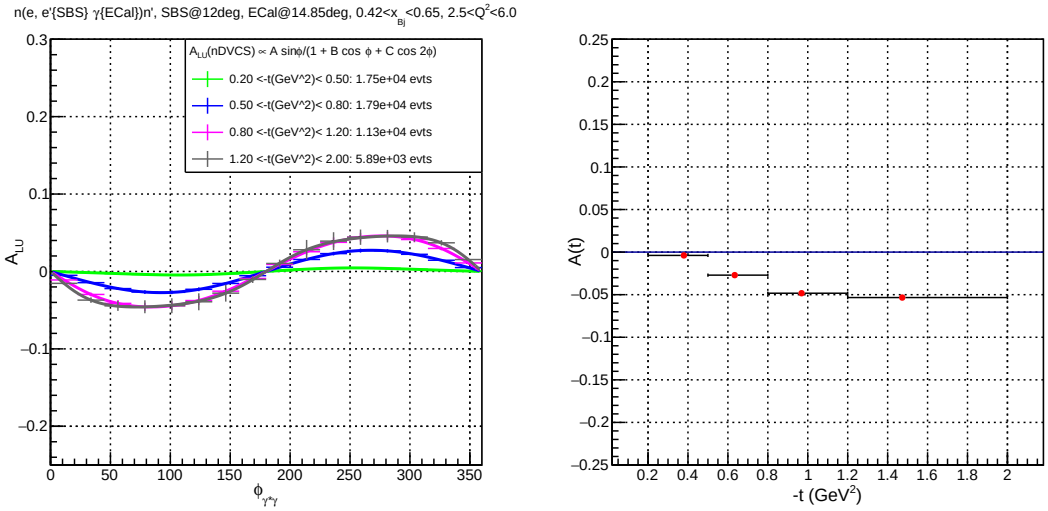

Figure 30: Projected DVCS beam spin asymmetry for the neutron as a function of $\phi_{\gamma\gamma}$ (left panels) and fitted $sin\phi$ component A (red dots) as a function of t (right panels) for our lower x_{Bj}, Q^2 bin (bin 5 on Fig. 27). The statistics for each t bin is indicated in the legend.

10 Summary

The neutron DVCS experiments provide a particularly important insight of the partonic structure of the nucleon, and this through three different approaches:

- The determination of the different contributions of n-DVCS observables (beam spin asymmetries mostly - the possibility to extract cross sections has to be fully investigated). That will allow to access combinations of GPD integrals which are complementary to the ones provided by proton experiments.
- The determination of the different contributions of d-DVCS observables. The study of d-DVCS process can reveal new nuclear effects and can be linked, within particular models, to nucleon GPDs.
- The determination of deeply virtual π^0 observables off the neutron. This measurement may also be linked to GPDs and is complementary to proton measurements.

The previous neutron DVCS experiments on deuterium, while bringing exciting physics results, taught us that a major source of systematic uncertainty is the separation between the proton and neutron events. The proposed experiment offers the possibility to reduce this uncertainty with the identification of the spectator proton, which will bring an enhanced knowledge of the measured quantities of interest linked to the partonic structure of the nucleon.

We would request to add a calorimeter during the TDIS experiment in order to record in parallel the n-DVCS and d-DVCS on deuterium target. To this end, we will add an existing high resolution electromagnetic calorimeter, such as the one used in the Neutral Particle Spectrometer (NPS).

References

[1] D. Mueller, D. Robaschik, B. Geyer, F. M. Dittes, and J. Horejsi, Fortschr. Phys. **42**, 101 (1994), hep-ph/9812448.

[2] A. V. Radyushkin, Phys. Rev. **D56**, 5524 (1997), hep-ph/9704207.

[3] X.-D. Ji, Phys. Rev. Lett. **78**, 610 (1997), hep-ph/9603249.

[4] L.L. Frankfurt, P.V. Pobylista, M.V. Polyakov and M. Strikman, Phys. Rev. **D60**, 014010 (1999).

[5] E.R. Berger, F. Cano, M. Diehl and B. Pire, Phys. Rev. Lett. **87**, 142302 (2001).

[6] A. Kirchner and D. Mueller, Eur. Phys. J. **C32**, 347 (2004).

[7] F. Cano and B. Pire, Eur. Phys. J. **A19**, 423 (2004).

[8] Jefferson Lab Hall A, C. Muñoz Camacho *et al.*, Phys. Rev. Lett. **97**, 262002 (2006), nucl-ex/0607029.

[9] Jefferson Lab Hall A, M. Mazouz *et al.*, To appear in Phys. Rev. Lett. (2007), nucl-ex/0709.0450.

[10] A. V. Belitsky, D. Mueller, and A. Kirchner, Nucl. Phys. **B629**, 323 (2002), hep-ph/0112108.

[11] E. Fuchey *et al.*, Phys. Rev. **C83**, 025201 (2011), 1003.2938.

[12] CLAS, I. Bedlinskiy *et al.*, Phys. Rev. **C90**, 025205 (2014), 1405.0988, [Addendum: Phys. Rev.C90,no.3,039901(2014)].

[13] Jefferson Lab Hall A, M. Defurne *et al.*, Phys. Rev. Lett. **117**, 262001 (2016), 1608.01003.

[14] Jefferson Lab Hall A, M. Mazouz *et al.*, Phys. Rev. Lett. **118**, 222002 (2017), 1702.00835.

[15] S. Niccolai, V. Kubarovsky, A. El Alaoui, M. Mirazita (spokespersons), Deeply Virtual Compton Scattering on the Neutron with CLAS12 at 11 GeV (2011).

[16] W. Armstrong, K. Hadifi, R. Dupré, Z.-E. Meziani (spokespersons), Spectator-Tagged Deeply Virtual Compton Scattering on Light Nuclei (2017), nucl-ex/1708.00835v1.

[17] C. Keppel, B. Wojtsekowski, P. King, D. Dutta, J.R.M. Annand, J. Zhang (spokespersons), Measurement of Tagged Deep Inelastic Scattering (TDIS): PR12-14-010 JLab experiment proposal (2014).

[18] B. Quinn, B. Wojtsekowski, R. Gilman (spokespersons), Precision Measurement of the Neutron Magnetic Form Factor up to $Q^2 = 18.0$ (GeV/c)^2 by the Ratio Method (2009).

[19] B. Wojtsekowski, G. Cates, S. Riordan (spokespersons), Measurement of the Neutron Electromagnetic Form Factor Ratio G_E^n/G_M^n at High Q^2 (2009).

[20] C. Perdrisat, L. Pentchev, E. Cisbani, V. Punjabi, B. Wojtsekowski (spokespersons), Large acceptance Proton Form Factor Ratio measurements at 13 and 15 (GeV/c)^2 using Recoil Polarization Method (2007).

[21] G. Cates, E. Cisbani, G. Franklin, A. Puckett, B. Wojtsekowski (spokespersons), Measurement of Semi-Inclusive Pion and Kaon electroproduction in the DIS Regime on a Transversely Polarized ^{3}He Target using the Super BigBite and BigBite Spectrometers in Hall A (2009).

[22] B. A. Mecking and others, Nucl. Inst. and Meth. **503**, 513 (2003).

[23] N. Akopov, Nucl. Instrum. Meth. **A479**, 511 (2002), physics/0104033.

[24] T. Horn, J. Phys.: Conf. Ser. **587**, 012048 (2014), nucl-ex/1708.00835v1.

[25] PrimEx, M. Kubantsev, I. Larin, and A. Gasparian, AIP Conf. Proc. **867**, 51 (2006), physics/0609201, [,51(2006)].

[26] PrimEx, A. Gasparian, A high performance hybrid electromagnetic calorimeter at Jefferson Lab, in *Calorimetry in particle physics. Proceedings, 11th International Conference, CALOR 2004, Perugia, Italy, March 29-April 2, 2004*, pp. 109–115, 2004.

[27] L. W. Whitlow, E. M. Riordan, S. Dasu, S. Rock and A. Bodek, Phys. Lett. B **282** (1992).

[28] M. Vanderhaeghen *et al.*, Phys. Rev. **C62**, 025501 (2000), hep-ph/0001100.

[29] M. Vanderhaeghen, P. Guichon and M. Guidal, Phys. Rev. **D60**, 094017 (1999).

[30] M. Vanderhaeghen, P. A. M. Guichon, and M. Guidal, Phys. Rev. **D60**, 094017 (1999), hep-ph/9905372.